Overview of Solar-Induced chlorophyll Fluorescence (SIF) from the Orbiting Carbon Observatory-2: Retrieval, cross-mission comparison, and global monitoring for GPP

Ying Sun[a,b,*], Christian Frankenberg[c,a,**], Martin Jung[d], Joanna Joiner[e], Luis Guanter[f], Philipp Köhler[c], Troy Magney[a]

[a] *Jet Propulsion Laboratory, California Institute of Technology, Pasadena, CA, United States*
[b] *School of Integrative Plant Science, Soil and Crop Sciences Section, Cornell University, Ithaca, NY, United States*
[c] *Division of Geological and Planetary Sciences, California Institute of Technology, Pasadena, CA, United States*
[d] *Max Planck Institute for Biogeochemistry, Jena, Germany*
[e] *NASA Goddard Space Flight Center, Greenbelt, MD, United States*
[f] *Helmholtz Centre Potsdam, German Research Centre for Geosciences, Potsdam, Germany*

ARTICLE INFO

ABSTRACT

The Orbiting Carbon Observatory-2 (OCO-2), launched in July 2014, is capable of measuring Solar-Induced chlorophyll Fluorescence (SIF), a functional proxy for terrestrial gross primary productivity (GPP). Although its primary mission is to measure the column-averaged mixing ratio of CO_2 (Xco_2) to constrain global carbon source/sink distribution, one of the OCO-2 spectrometers allows for a robust SIF retrieval solely based on solar Fraunhofer lines. Here we present a technical overview of the OCO-2 SIF product, aiming to provide the scientific community guidance on best practices for data analysis, interpretation, and application. This overview consists of the retrieval algorithms, OCO-2 specific bias correction, retrieval uncertainty evaluation, cross-mission comparison with other existing SIF products, and a global-scale examination of the SIF-GPP relationship. With the initial three years of data (September 2014 onward), we compared OCO-2 SIF with retrievals from Greenhouse Gases Observing Satellite (GOSAT) and Global Ozone Monitoring Experiment-2 (GOME-2), and examined its relationship with FLUXCOM and MODIS GPP datasets. Our results show that OCO-2 SIF, along with GOSAT products, closely resemble the mean spatial and temporal patterns of FLUXCOM GPP from regions to the globe. Compared with GOME-2, however, OCO-2 depicts a more realistic spatial contrast between the tropics and extra-tropics. The linear relationship between OCO-2 SIF and existing modeled GPP products diverges somewhat across biomes at the global scale, consistent with previous GOSAT or GOME-2 based findings when modeled GPP products were used, but in contrast to a consistent cross-biome SIF-GPP relationship obtained at flux tower sites with OCO-2 products. This contrast suggests a critical need to reconcile differences in diverse SIF and GPP products and the relationships among them. Overall, the OCO-2 SIF products are robust and valuable for monitoring the global terrestrial carbon cycle and for constraining the carbon source/sink strengths of the Earth system. Finally, insights are offered for future satellite missions optimized for SIF retrievals.

1. Introduction

Satellite measurements of steady-state Solar-Induced chlorophyll Fluorescence (SIF) open up a new avenue for monitoring terrestrial gross primary productivity (GPP) from space (Frankenberg et al., 2011b; Guanter et al., 2012; Joiner et al., 2013; Jung et al., 2011; Köhler et al., 2015; Y. Sun et al., 2017). Detecting SIF is also critical to accurate retrievals of trace gases such as column-averaged dry-air mole fraction of CO_2 (i.e., Xco_2) (Frankenberg et al., 2012, 2011a). Global retrievals of satellite SIF have been achieved at various wavelengths with multiple space-borne instruments (Frankenberg et al., 2011b; Guanter et al., 2012; Joiner et al., 2013, 2011; Köhler et al., 2015). Existing instruments include the Fourier Transform Spectrometer (FTS) onboard the Japanese Greenhouse Gases Observing Satellite (GOSAT), the Global Ozone Monitoring Experiment-2 (GOME-2) onboard the European MetOp-A and MetOp-B, the SCanning Imaging Absorption

spectroMeter for Atmospheric CHartographY (SCIAMACHY) onboard ENVISAT, the Orbiting Carbon Observatory-2 (OCO-2), and the TROPOspheric Monitoring Instrument (TROPOMI) onboard Sentinel-5 Precursor (S5p).

The general principle for retrieving SIF is based on the in-filling of solar Fraunhofer lines, i.e., measuring the fractional depth of the Fraunhofer lines, which decreases in the presence of SIF emission from the Earth surface. This approach was originally proposed by Plascyk and Gabriel (1975) and evaluated by the in-filling of luminescence in a single deep Fraunhofer line. The first global SIF retrieval was achieved with GOSAT-FTS, by evaluating the in-filling of Fraunhofer lines located around 755 nm and 771 nm where the contamination from atmospheric scattering and absorption is minimized (Joiner et al., 2011; Frankenberg et al., 2011b; Guanter et al., 2012). The high spectral resolution of GOSAT-FTS (~0.025 nm) allows for resolving the narrow and isolated solar Fraunhofer lines, ensuring a robust and accurate retrieval. However, GOSAT has poor spatial and temporal data sampling. It acquires only one spectrum every 4 s and individual orbital tracks are hundreds of kilometers apart. This drawback hinders the continuous global mapping of SIF with GOSAT. Subsequent studies using GOME-2 and SCIAMACHY (Joiner et al., 2013, 2012; Köhler et al., 2015; Wolanin et al., 2015) showed that it is also possible to retrieve SIF with moderate spectral resolutions (~0.5 nm) by spectral fitting with a broad spectral window. Using a statistical approach based on principal component analysis (PCA) or singular value decomposition (SVD), SIF was inferred at 740 nm by fitting the window of 734–758 nm (Joiner et al., 2013) or 720–758 nm (Köhler et al., 2015). The PCA technique simplified the atmospheric radiative transfer modeling and enabled disentangling the spectral signatures of atmospheric absorption, surface reflectance, and fluorescence emission (Joiner et al., 2013). Although a broad spectral window fitting poses a challenge for completely eliminating the atmospheric impact on SIF, continuous spatial mapping became possible across the globe (Joiner et al., 2013; Köhler et al., 2015). In addition to the abovementioned efforts that focus on the far-red SIF retrieval, Joiner et al. (2016) developed a novel approach to estimate the SIF emission at the red spectral region. This approach utilizes the O_2 γ-band, which is relatively SIF free, to constrain the atmospheric impact on the absorption within the O_2 B band, thus isolating SIF in the O_2 B band from effects of scattering. This strategy improves the retrieval precision of red SIF as compared with fitting only Fraunhofer lines in the vicinity of the O_2 B band.

The availability of these SIF datasets has spurred a considerable number of applications of SIF to understand terrestrial ecosystem dynamics. Accurate interpretation and process attribution with SIF depend on specific data characteristics of each instrument (resolutions, retrieval precision, observational geometry, etc.). Such technical information has been provided for GOSAT (e.g., Frankenberg et al., 2011a, 2011b; Guanter et al., 2012), GOME-2 (e.g., Joiner et al., 2013; Köhler et al., 2015), and SCIAMACHY (e.g., Köhler et al., 2015). However, a comprehensive description of the OCO-2 SIF product is not yet provided to the community since OCO-2's launch in September 2014, although a growing number of OCO-2 SIF based studies have already been published recently (Köhler et al., 2017; Li et al., 2018; Y. Sun et al., 2017; Verma et al., 2017; Wood et al., 2017). This study aims to provide a technical overview of the OCO-2 SIF retrieval, in order to help users understand the data quality, advantage and limitations relative to other existing products. For this purpose, this paper will use the operational collection of OCO-2 measurements, different from Frankenberg et al. (2014), which used pre-launch synthetic simulations to assess the radiometric performance of the instrument. Y. Sun et al. (2017) has summarized the unique new research opportunities enabled by OCO-2 SIF, and this present paper focuses on the technical details of this dataset.

The paper is structured as follows: Section 2 provides a technical description of the OCO-2 SIF products, consisting of an OCO-2 mission overview, the retrieval algorithm, instrument "offset" correction, and quality control. Note the retrieval algorithm (Section 2.2) is not OCO-2 specific but is identical to the one implemented for GOSAT. It can also readily be applied to future missions that employ spectrometers of similar characteristics. It is included here for the sake of completeness to benefit readers. The correction of instrument artifacts (Section 2.5) is a critical step specific to the OCO-2 grating spectrometers and has to be carefully accounted for to ensure unbiased SIF retrieval. Section 3 describes the cross-comparison schemes among different missions that have the capability for SIF retrieval. Section 4 reports the results on the SIF cross-mission comparison and on the SIF-GPP relationships. The latter aspect has been intensively investigated for GOSAT and GOME-2, thus not inherently new to OCO-2; but it is included in this overview paper so that the SIF community can gain a complete picture about the OCO-2 SIF product and its capability/limitations in constraining GPP.

2. Description of the OCO-2 SIF product

2.1. The OCO-2 mission

OCO-2 flies in a sun-synchronous orbit with a local overpass time at 1:30 pm. The instrument consists of three grating spectrometers, recording high-resolution radiance spectra in three bands: the O_2-A band (757–775 nm, Full Width at Half Maximum FWHM = 0.042 nm), a weak CO_2 absorption band (1594–1627 nm, FWHM = 0.076 nm), and a strong CO_2 absorption band (2043–2087 nm, FWHM = 0.097 nm). The O_2-A band spectrometer is utilized for OCO-2 SIF retrieval as it 1) overlaps with the SIF emission spectrum (i.e., 660–850 nm) and 2) covers a few relatively deep solar Fraunhofer lines. Each spectrometer provides eight independent cross-track spectra, with each spectrum having a nominal spatial resolution of $1.3 \times 2.25 km^2$ (denoted as footprint) at nadir. These footprints together cover a maximum ~10 km-wide full swath. Note that due to slit rotation, the effective swath narrows near the equator, where eight footprints repeat the same ground pixel as the slit is aligned exactly along track.

In the original configuration, the viewing geometry of OCO-2 alternates every 16 days (instrument repeat cycle) between nadir and glint modes. Since July 2nd, 2015, the satellite viewing modes alternate from orbit to orbit, not between repeat cycles. The nadir mode follows a similar ground track during each repeat cycle, allowing for a reliable detection of variations over time. Compared to the glint mode, the nadir mode typically provides a slightly higher spatial resolution, a better signal-to-noise ratio (SNR) over land, and more useful soundings in regions impacted by clouds or with significant topography. The glint mode, relative to nadir, has varying east-west offsets. Spectra acquired from the glint mode have significantly higher SNR over the dark ocean (especially at high latitudes) due to the "bright" specular reflectance of solar radiation. Over land, however, glint measurements may underestimate SIF compared to nadir, because a more shaded fraction of the canopy may be observed (Frankenberg et al., 2014). In addition to the nadir and glint modes, there is a target mode which is occasionally switched on when the satellite overpasses ground validation sites. In this mode, a large number of temporally continuous measurements at different viewing zenith angles (VZA) is made, enabling research into the bidirectional effect of SIF. The present paper focuses on nadir spectra, as they provide the most consistent measurements in time.

The OCO-2 spectrometers acquire 24 spectra per second, an almost 100-fold increase in data acquisition frequency over GOSAT (one spectrum every 4 s). The spatial resolution of OCO-2 nominal footprint is $1.3 \times 2.25 km^2$, much finer than GOSAT, GOME-2, and SCIAMACHY (Table 1 and Y. Sun et al., 2017). On average, OCO-2 acquires > 10^5 clear-sky soundings on land per day, a considerable increase in data acquisition. These marked improvements of OCO-2 enable more in-depth SIF-related studies than previously possible, for example, improved validation with ground measurements and detection of small-scale eco-physiological changes (Y. Sun et al., 2017). The sampling strategy, however, comes at a cost of spatial contiguity, as OCO-2 does

Table 1
Technical details of SIF and GPP products used in this study.

	SIF			GPP	
	OCO-2[b]	GOSAT-FTS	GOME-2/MetOp-A	FLUXCOM	MODIS
Temporal coverage	09/2014 to present	04/2009 to present	01/2007 to present	2009 to 2015	2000 to 2015
Spatial resolution for global gridded mapping	$1° \times 1°$ (monthly)	$2° \times 2°$ (monthly)	$0.5° \times 0.5°$ (monthly)	$0.083° \times 0.083°$ (8-day)	$0.05° \times 0.05°$ (monthly)
Spatial resolution of ground footprint	$1.3 \times 2.25\,km^2$	10 km diameter	$40 \times 40\,km^{2a}$	–	–
Repeat cycle	16 days	3 days	3 days[a]	–	–
Number of clear-sky soundings per month on land	~2.000,000 (nadir)	~20,000	~80,000	–	–
Local overpass time	1:30 pm	1:00 pm	9:30 am	–	–
Spectral resolution	~0.05 nm	~0.025 nm	~0.5 nm	–	–
Fitting window	Micro-windows at 757 nm and 771 nm	Micro-windows at 755 nm and 771 nm	Broad window from 734 nm (or 720 nm) to 758 nm[c]	–	–

[a] Since July 15th 2013, the pixel size of ground footprint is reduced to $40 \times 40\,km^2$ (from $40 \times 80\,km^2$) and the repeat cycle is increased to 3 days (from 1.5 days), associated with the swath-width reduction of GOME-2 onboard MetOp-A.

[b] Analysis in this study includes data up to April 2016.

[c] GOME-2 v26 products (Joiner et al., 2013) use a fitting window of 734–758 nm, while GOME-2 GFZ products (Köhler et al., 2015) use a fitting window of 720–758 nm.
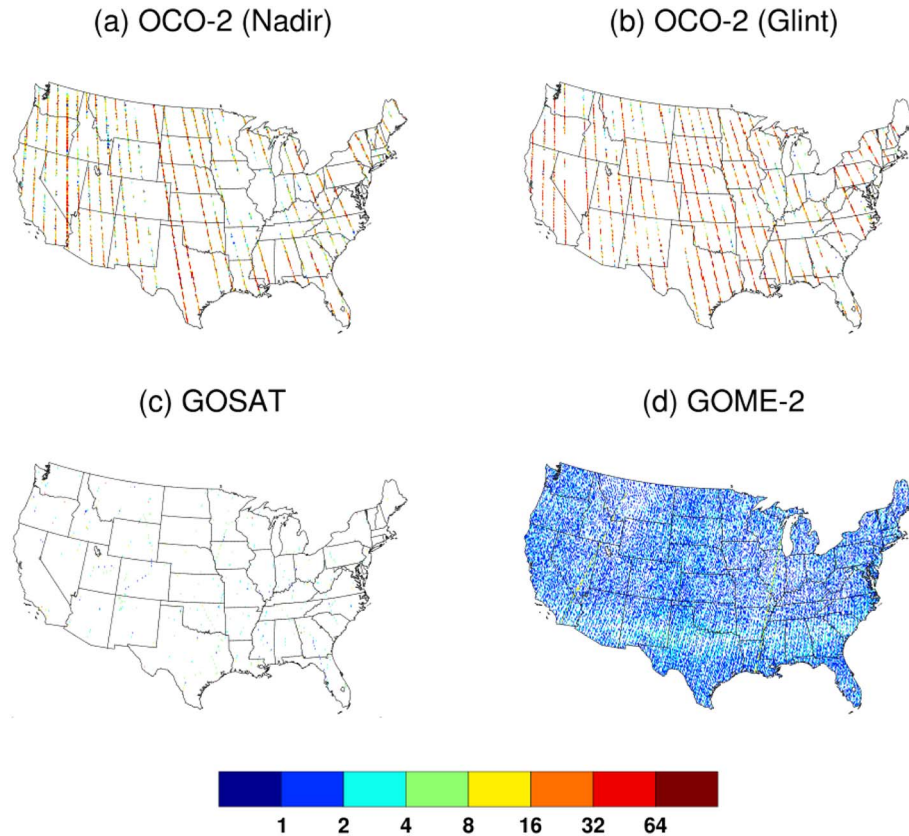

Fig. 1. Illustration of the spatial distribution of the data acquisition, i.e., the number of soundings (represented by colors), of OCO-2, GOSAT-FTS, and GOME-2 onboard MetOp-A, using July 2015 as an example. The level 2 retrieval is aggregated to $0.1° \times 0.1°$, roughly equivalent to the OCO-2 swath widths (~10 km) in mid-latitude such as US.

not provide full global coverage with its 10 km-wide swath (Fig. 1). The specific characteristics of OCO-2 and comparison to other instruments are provided in Table 1.

2.2. The SIF retrieval algorithm

The OCO-2 SIF retrieval is solely based on in-filling of solar Fraunhofer lines in narrow spectral windows around 757 nm and 771 nm. The rationale of using Fraunhofer lines is that atmospheric scattering due to aerosols or thin clouds has no impact on the depth of isolated Fraunhofer lines. The original algorithm was developed for

GOSAT SIF retrieval and has been adapted for OCO-2 (Frankenberg et al., 2012, 2011a). The adaptation is facilitated by the fact that OCO-2 and GOSAT share similar spectral coverage and resolution in the 757–772 nm window encompassing a large number of Fraunhofer lines at both sides of the O_2-A band. The retrieval algorithm is described below.

For a Lambertian target, the spectral radiance measured by a sensor at TOA at wavelength λ can be approximated as:

$$L_{TOA}^\lambda = I_0^\lambda \cdot \mu \cdot \left(\rho_0^\lambda + \rho_s^\lambda \cdot \frac{T_\downarrow^\lambda \cdot T_\uparrow^\lambda}{\pi} \right) + SIF_{TOA}^\lambda$$
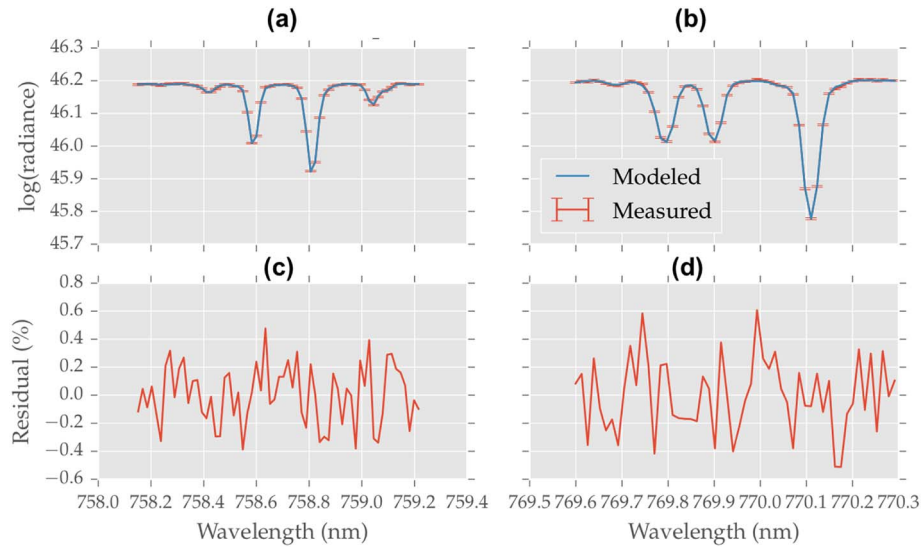
(1)

Fig. 2. The fitted spectra and fitting residuals for the 757 nm (left) and 771 nm (right) micro-windows of OCO-2 soundings in Australia (October 7th, 2016, 32.89439˚S, 148.13908˚E). The error bar of the measured spectra represents the estimated single measurement precision (i.e., σ_i) for each OCO-2 sounding, as provided in the Level 1 dataset.

where I_0^λ is the extraterrestrial solar irradiance, μ is the cosine of the solar zenith angle (SZA), ρ_0^λ is the atmospheric path reflectance, ρ_s^λ is the surface reflectance, $T_\downarrow^\lambda$ and $T_\uparrow^\lambda$ are total atmospheric transmittance (both diffuse and direct) in the down-welling and up-welling directions; SIF_{TOA}^λ is the SIF emission at TOA.

In the absence of inelastic atmospheric scattering (such as rotational Raman scattering RSS, Vasilkov et al., 2013) and narrow atmospheric absorption features overlapping with the Fraunhofer lines, the fractional depth of Fraunhofer lines remain invariant to elastic scattering within the atmosphere (ρ_0^λ, $T_\downarrow^\lambda$, and $T_\uparrow^\lambda$) and from the Earth surface (ρ_s^λ). The primary reason why the fractional depth is invariant is that all atmospheric or surface scattering events are spectrally smooth multiplicative processes, not changing the ratio of the Fraunhofer line core vs. the continuum level radiance. Therefore, within narrow microwindows (< 1 nm wide), these scattering terms $\mu \bullet \left(\rho_0^\lambda + \rho_s^\lambda \bullet \frac{T_\downarrow^\lambda \bullet T_\uparrow^\lambda}{\pi} \right)$ can be approximated by a low-order polynomial in λ, i.e., $\sum_{i=0}^n a_i \bullet \lambda^i$. This assumption is valid as long as the fitting window is devoid of spectrally sharp atmospheric absorption. With this assumption, the forward model can be written as:

$$L_{TOA}^\lambda (SIF_{TOA}^\lambda, \boldsymbol{a}) = \langle I_0^\lambda \rangle \bullet \sum_{i=0}^n a_i \bullet \lambda^i + SIF_{TOA}^\lambda \qquad (2)$$

where $< >$ is the convolution operator, convolving the very high-resolution I_0^λ input spectrum with the instrument line-shape. The first term models the variation of continuum level radiance (at low frequency) due to the surface reflectance and the atmospheric continuum absorption as described above. The second term is TOA SIF, which is assumed to be spectrally constant within a narrow fitting window in the far-red spectral region; therefore, a prescribed SIF spectral shape is not required as a priori. Specific to GOSAT and OCO-2, the forward model is expressed in logarithmic form:

$$\vec{f}(SIF^{rel}, \boldsymbol{a}) = \log(\langle \vec{I_0} + SIF^{rel} \rangle) + \sum_{i=0}^n a_i \bullet \lambda^i \qquad (3)$$

where SIF^{rel} is a unitless quantity characterizing the relative contribution of SIF to the continuum level radiance and $\vec{I_0}$ a disk-integrated solar transmission model. The retrieved parameters are SIF^{rel} and the vector $\boldsymbol{a}$ consisting of the polynomial coefficients a_i ($i = 0, 1, 2$). Once SIF^{rel} is retrieved, SIF in radiance unit is derived using $SIF = SIF^{rel} \cdot R_{cont}$ where R_{cont} is the continuum level radiance within the fitting window. Eq. (3) could in principle be solved with a simple linear least squares

technique. However, we also fit spectral shift and squeeze, which requires a non-linear least-square optimization to minimize the spectral residual between the measured radiance and the forward model (Frankenberg et al., 2011a). In principle, this could be done in a two-step process (Köhler et al., 2015) but we optimize SIF, spectral alignment and polynomial coefficients in a joint non-linear inversion. The least-square fitting is performed independently for two micro-windows: 758.1–759.2 nm and 769.6–770.3 nm windows, respectively (Fig. 2). Traditionally the former is referred to as the 757 nm window while the latter the 771 nm window (e.g., Frankenberg et al., 2014), and we keep this notation here for consistency. Fig. 2 shows example fits for both windows. The modeled spectra with the forward model Eq3 accurately fit the measured spectra within the noise level in both windows, reproducing the fractional depth of all individual Fraunhofer lines.

It is important to note that in the solar Fraunhofer lines, the atmosphere is almost transparent $T_\uparrow^\lambda \approx 1$ for near-nadir observations under clear-sky conditions (Guanter et al., 2012), therefore SIF_{TOA}^λ approximates SIF_{TOC}^λ. Even in scattering atmospheres with low scattering optical depth, the effective transmission is close to 1 because the scattered SIF radiance is preserved in the diffuse radiation and still contributes to TOA radiance in the absence of severe absorbing aerosol loadings. In fact, Frankenberg et al. (2012) used a full-physics radiative transfer model to demonstrate that, at nadir, the ratio of TOA and TOC SIF is close to unity under clear skies, and well above 0.8 if the total aerosol and cloud optical depth is lower than 1. This model-based finding is further corroborated by actual measurements of GOSAT, which show minimal differences between TOA and TOC SIF under varying degree of aerosol loadings. However, the cloud-surface multiple interactions as well as absorbing aerosols might have an impact on the escape probability of TOC SIF to TOA. But in this case, the incoming PAR that triggers SIF emission is reduced by an even larger amount under cloudy skies anyway. As the OCO-2 SIF product has been undergoing a cloud-screening procedure (Section 2.3), SIF values affected by absorbing aerosols/thick clouds are already excluded and the provided TOA SIF data represent TOC SIF very well. On the other hand, such cloud screening procedure might create a clear-sky bias in the observed SIF signals, which warrants further investigations and needs to be considered by researchers using SIF products from space in general.

2.3. Quality control

The retrieved SIF is further screened according to the following
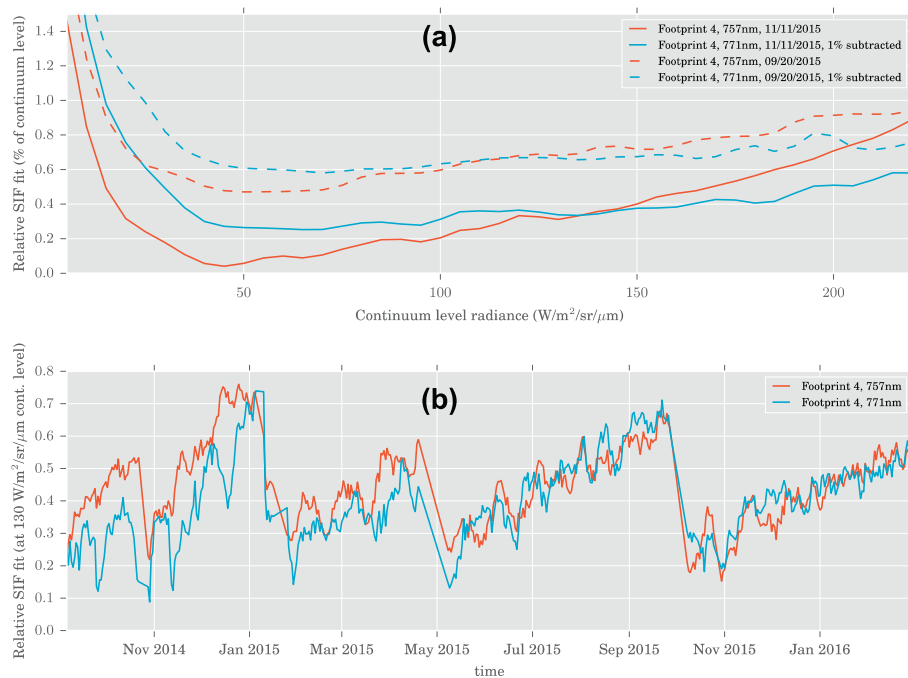
Fig. 3. Correction of instrument artifacts. (a) Raw SIF retrievals (i.e., SIF^{rel}, relative SIF signal as a percentage to the continuum level radiance) as a function of continuum level radiance over non-fluorescing surfaces for two different days and wavelengths. (b) The time dependence of the offset around $130 \, \text{Wm}^{-2} \, \mu\text{m}^{-1} \, \text{sr}^{-1}$ of continuum level radiance.

quality criteria:

1) The reduced χ^2 of the retrieval residuals in the range of 0 to 2 (to exclude unsuccessful retrievals). Here the reduced χ^2 is a metrics of the goodness of fit for the retrieval, which is defined as the χ^2 (i.e., the ratio of the weighted sum of the deviation between observations and the forward model calculation against the variance of observation) per degree of freedom (i.e., the difference between the number of observations and the number of fitted parameters).
2) The continuum level radiance in the range of 28 and $195 \, \text{Wm}^{-2} \, \mu\text{m}^{-1} \, \text{sr}^{-1}$ (to remove scenes that are too dark or too bright).
3) The solar zenith angle $< 70°$ (to exclude retrievals affected by high air mass, for which rotational-Raman scattering may lead to positive bias).
4) The ratio of retrieved vs. predicted column O_2 in the range of 0.85 to 1.5 (to exclude cloudy scenes).
5) The ratio of column CO_2 retrieved in the weak vs. strong CO_2 band in the range of 0.5 to 4.0 (to exclude cloudy scenes). Details of the cloud screening algorithm of OCO-2 can be found elsewhere (Taylor et al., 2016).

2.4. Correction of instrumental artifacts

One of the primary systematic error sources of SIF measurements using Fraunhofer lines stems from imperfect knowledge of instrument condition and its changes over time, especially those related to either changes in the instrumental line shape or anything that can mimic an additive signal such as SIF. For instance, for GOSAT spurious fluorescence signals over bright ice surface were initially detected but could be traced back to a so-called zero-level offset in the recorded interferogram (Frankenberg et al., 2011b). In this case, a non-linearity in the interferogram acquisition at zero path difference is propagated into an additive offset in spectral space, a feature that fills in Fraunhofer lines in exactly the same way as SIF does. To correct for this feature of GOSAT, a parameterization of spurious in-filling as a function of total signal level was developed on a monthly basis. OCO-2 is a grating spectrometer and as such is not susceptible to this type of zero-level offsets.

However, other instrument features come into play: 1) a small error in the assumed instrument line-shape or the solar transmission model can result in a constant error in relative fluorescence, 2) residual non-linearities in the signal response can create a signal-level dependent relative offset, and 3) straylight can mimic an additive offset, which should also remain constant in relative fluorescence if the same percentage of overall light level is scattered and reaches the detector as straylight.

For these reasons and the experience from GOSAT retrievals, we also implemented a SIF correction scheme, which is parameterized as a function of continuum radiance for OCO-2. Given the much higher data volume for OCO-2, we decided to parameterize correction schemes on a daily basis, as opposed to monthly for GOSAT. For this correction scheme, all supposedly non-fluorescing soundings (barren surfaces, oceans, ice and snow-covered areas) were collected for each day and SIF^{rel} was binned by overall continuum level radiance. Fig. 3a shows the SIF offset correction curves for two different days and micro-windows. It shows that there is some signal level dependence of bias correction in SIF^{rel}, especially at low radiance levels but also towards higher levels, particularly for the 757 nm spectral window. This might be related to a small detector non-linearity but we note that this finding is empirical. It can also be seen that this overall behavior changes in time but appears to be like an overall vertical shift in magnitude rather than a change in the particular shape of the curve (comparing the solid and dash lines recorded on different dates in Fig. 3a). This points to the following: the signal level dependence remains rather constant but the overall offset, which could be related to instrument line-shape or straylight issues, varies in time.

The time dependence of the offset around $130 \, \text{Wm}^{-2} \, \mu\text{m}^{-1} \, \text{sr}^{-1}$ of continuum level radiance is shown in Fig. 3b. A strong temporal dependency of the correction scheme can be observed, which is consistent with findings by K. Sun et al. (2017), who investigated changes in the instrument line shape over time. The current explanation for this behavior is that there is a slow buildup of a thin ice layer on top of the focal plane array of the O_2 A-band detector (K. Sun et al., 2017). This ice layer causes scattered straylight across the detector and also a concurrent degradation of the detector response, which is already corrected by the Level 1 to Level 2 processing. Supporting evidence for

this explanation comes from the fact that there is a sudden jump in the offset after decontamination cycles, which were initially intended to reduce the overall loss in throughput. The ice layer is supposed to cause spectral straylight, which has the same effect on the depth of Fraunhofer lines as SIF. In hindsight, the choice of a daily correction scheme was fortunate as there seem to be temporally variable contributing factors, which would have propagated into biases if we had chosen a monthly scheme. Further work can improve our methods though, especially through investigations of glint vs. nadir observations or different choices of reference targets.

2.5. Uncertainty assessment

A full validation includes rigorous testing of not only the SIF magnitude itself but also the reliability of the provided uncertainty estimates. OCO-2 SIF data provided to users include both SIF and the corresponding single measurement precision, denoted as σ_i, the random component of the retrieval errors (where i is the index of a single sounding). σ_i is derived directly by the standard least-square fitting, through evaluating the retrieval error covariance matrix $S_e = (K^T S_0 K)^{-1}$, where K is the Jacobian matrix from the least-square fit, and S_0 is the measurement error covariance matrix characterizing the instrument noise. Typically, σ_i varies between 0.3 and 0.5 $Wm^{-2}\mu m^{-2}sr^{-1}$ (15–25% of typical peak values of SIF) in the 757 nm fitting window (Frankenberg et al., 2014), but the error would be substantially reduced by a factor of $1/\sqrt{n}$ if single retrievals (from individual soundings) are binned to gridded maps (n is the number of soundings per gridcell) at certain temporal averaging domains. We assessed the retrieval error of the grid-averaged SIF in two ways. First, we calculated the theoretical standard error based on σ_i as provided in the OCO-2 data product. This theoretical standard error (denoted as σ_{theo}) at each grid-cell is calculated as follows (Frankenberg et al., 2011b):

$$\sigma_{theo} = \frac{1}{\sqrt{\sum_{i=1}^{n} (1/\sigma_i^2)}}. \tag{4}$$

Second, we computed the actual measured standard error of the mean (denoted as σ_{meas}), using

$$\sigma_{meas} = \frac{\sigma_{std}}{\sqrt{n}} \tag{5}$$

Here σ_{std} is the standard deviation of the n soundings within a grid-cell, calculated by $\sigma_{std} = \sqrt{\frac{\sum_{i=0}^{n} (SIF_i - SIF_m)^2}{n}}$ where SIF_i is the retrieved SIF for a single sounding, and SIF_m is the mean of all individual soundings. The two error metrics differ in that σ_{theo} quantifies the retrieval error originating only from instrument noise, while σ_{meas} characterizes both instrumental noise and spatial-temporal variability of all soundings within a given grid-cell (in our case $1° \times 1°$) and time frame (monthly). If the retrieval error is purely random and dominated by the instrument noise, σ_{theo} and σ_{meas} should be identical and thus positively correlated. Their relationship can be seen clearly in the Sahara where both spatial heterogeneity and temporal variability are minimized and instrument noise dominates the retrieval uncertainty (Fig. 4). In this relatively homogeneous region, σ_{meas} and σ_{theo} are tightly correlated ($R^2 = 0.95$) and closely follow (although slightly above) the 1:1 line indicating a similar magnitude between them. This suggests that the retrieval algorithm is able to produce a reliable error estimate, which ensures that most error sources are properly characterized by the retrieval process. The σ_{meas} values are slightly higher than those of σ_{theo} due to subtle variations of SIF across space and time used for spatial and temporal aggregation. Note that here we focus on the random retrieval error (or precision), as the systematic retrieval error (or accuracy) is generally small, i.e., $< 0.05\ Wm^{-2}\mu m^{-1}sr^{-1}$ (Frankenberg et al., 2014), after the correction of instrumental artifacts (Section 2.5).

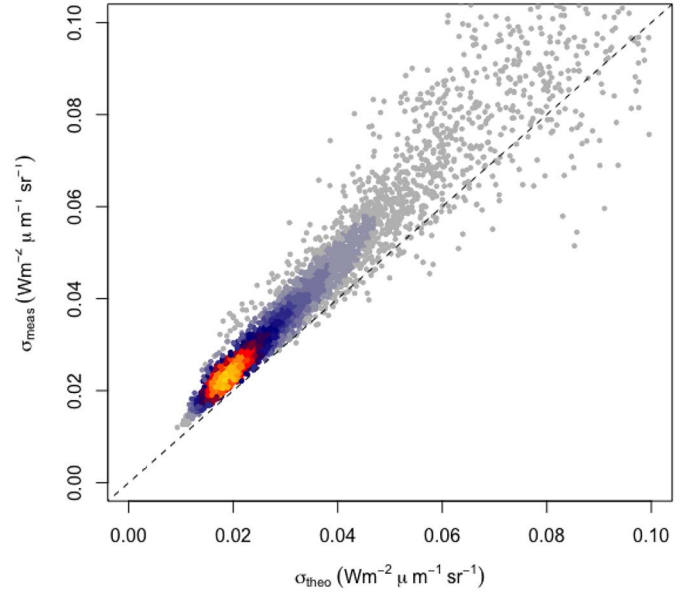**Fig. 4.** The relationship between σ_{meas} (y-axis) and σ_{theo} (x-axis) of OCO-2 SIF in the Sahara region (18°–28°N, 5°W–30°E). Scatters represent monthly values since September 2014, with color depicting the density of scatters. The dash line depicts the 1:1 line.

2.6. Generation of monthly gridded OCO-2 SIF

In this study, we primarily used the OCO-2 v8 product (B8100), which is delivered as Lite files on a daily basis. Each file contains SIF related fields for individual soundings within a single day. These SIF related fields include SIF retrievals at two micro-windows centered at 757 nm and 771 nm, labeled as SIF_{757} and SIF_{771}, respectively. Also included in each daily file are the corresponding single measurement precision $\sigma_{i,\ 757}$ and $\sigma_{i,\ 771}$ and the fitting-window specific continuum level radiance. Unless otherwise specified, the SIF value used in this study is the average of SIF values at 757 nm and 771 nm, with the latter multiplied by a factor of 1.5 because the value at 771 nm is typically ~1.5 times lower than that at 757 nm (detailed discussion in Section 4.1). The rationale for averaging the two wavelengths is to reduce the retrieval error (by a factor of $\sqrt{2}$) by doubling the number of soundings used for spatial-temporal averaging. The retrievals for the two micro-windows are affected by different uncertainties because they are performed independently. Therefore, averaging the two wavelengths could improve robustness in the data analysis. For comparison with other datasets, we binned the daily OCO-2 SIF products to monthly values at $1° \times 1°$ for global mapping. This spatial-temporal aggregation only includes successful retrievals under nadir mode that fulfill the filter criteria (i.e., Section 2.3). Despite the large gaps between individual orbits, there is a sufficient number of soundings in each monthly $1° \times 1°$ bin to ensure a robust signal of the grid-average SIF. Indeed, Frankenberg et al. (2014) demonstrated that the orbital gaps only incur a small bias on regional averages.

3. Evaluation methods

We evaluated the OCO-2 SIF datasets against independent SIF products including GOME-2 (2007–present, Joiner et al., 2013; Köhler et al., 2015) and GOSAT retrievals (April 2009–present, Frankenberg et al., 2011b) (Table 1). The far-red SIF (inferred at 740 nm using a broad fitting window of 734–758 nm) of GOME-2 onboard the MetOp-A is used in this study, with data filtered out if their effective cloud fraction is larger than 0.3 or the solar zenith angle (SZA) > 70°. Measurements with high SZA were excluded because RSS increases at high SZA and may lead to non-negligible positive bias. We used the GOME-2 v26 Level 3 products, which provide monthly global SIF coverage at
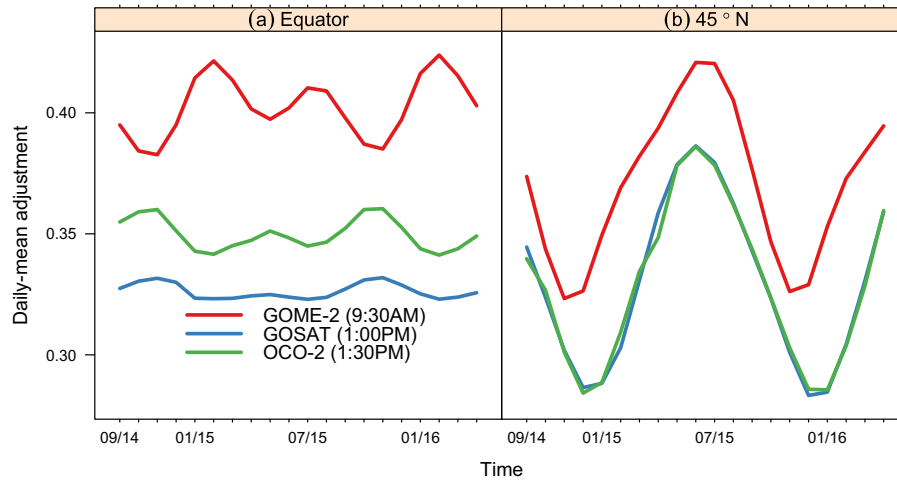
Fig. 5. The temporal variation of daily-mean adjustment of OCO-2, GOSAT, and GOME-2 along the latitudinal transects of (a) equator and (b) 45°N, respectively. The curves are derived by averaging all the acquired soundings within the same latitudinal transects.

0.5° × 0.5° spatial resolution. In addition, we included another GOME-2 product developed at German Research Center for Geosciences (GFZ) (Köhler et al., 2015). This product used a backward elimination algorithm to automatically optimize the number of fitted coefficients, unlike a fixed number of coefficients used by GOME-2 v26. Another major difference is a wider fitting window (i.e., 720–758 nm) of the GFZ product with respect to GOME-2 v26.

The GOSAT SIF retrieval is inferred at 757 nm and 771 nm at both P- and S-polarization (Frankenberg et al., 2011b). The GOSAT retrieval algorithm shares a similar strategy to OCO-2, but has a slightly wider fitting window for the 755 nm retrieval, which encompasses two more solar Fraunhofer lines. This is because the GOSAT-FTS covers 755–775 nm, which is shifted by two nanometers towards the shorter wavelength region compared to the OCO-2 spectrometer (i.e., 757–775 nm). We applied quality control filters to GOSAT SIF following Frankenberg et al. (2011b) to eliminate retrievals that are cloud contaminated or with high solar zenith angles. The GOSAT SIF values used for cross-mission comparison are the composite averages of the two wavelengths and two polarizations, with the 771 nm retrievals multiplied by a factor of 1.6 (more discussion in Section 4.1). Averaging these independent retrievals improves the robustness of SIF values, similar to the averaging strategy for OCO-2. We finally aggregated SIF from individual soundings to 2° × 2° on monthly scales to ensure sufficient data sampling for spatial-temporal averaging.

We examined the relationship of OCO-2 SIF to GPP products from both the Moderate Resolution Imaging Spectroradiometer (MODIS) MOD17A2 (www.ntsg.umt.edu, Zhao and Running, 2010) and FLUXCOM (www.fluxcom.org) (Tramontana et al., 2016), a successor of the MPI-BGC product (Jung et al., 2011) (Table 1). The MODIS GPP product is derived from an empirical light use efficiency model driven by MODIS measurements of fPAR (fraction of Photosynthetically Active Radiation)/LAI (Leaf Area Index) in conjunction with meteorological reanalysis datasets (Zhao and Running, 2010). The monthly gridded MODIS GPP is provided at 0.05° spatial resolution from 2000 to 2015 across the globe. We spatially aggregated this high resolution dataset to 1° × 1° to maintain consistency with OCO-2. The FLUXCOM GPP product is derived from training three machine learning algorithms with in-situ data from 224 FLUXNET sites and predictor variables obtained from an extensive variable selection analysis (Tramontana et al., 2016). The predictor variables are based exclusively on satellite based remote sensing data ("RS" setup in Tramontana et al., 2016) which allow for a relatively high spatial resolution (0.0833°), an 8-daily temporal resolution. Details for this GPP product along with a thorough site-level validation are given in Tramontana et al. (2016). Similar to MODIS GPP, we aggregated FLUXCOM GPP to 1° × 1° to maintain its

consistency with OCO-2.

To perform cross-mission comparison and to investigate SIF-GPP relationships, we applied a daily-mean adjustment to convert the instantaneous SIF at the local overpass time to the corresponding daily mean value, i.e., $\overline{SIF}$. The rationale for this is two-fold: a) the GPP products are the monthly mean of daily integrals, instead of a single measurement at a specific time, and b) such normalization eliminates the impact of varying incident solar radiation intensities due to different overpass times. Following Frankenberg et al. (2011b), the daily-mean adjustment d is formulated as:

$$d = \frac{\int_{t=t_0}^{t=t_0+1} \cos[SZA(t)] \cdot dt}{\cos[SZA(t_0)]}. \tag{6}$$

where t_0 is the time of measurement in fractional days, hence integration of cos (SZA) from t_0 to $t_0 + 1$ denotes a daily integral (nighttime data, i.e. negative cos(SZA) are zeroed out). We used pyEphem (http://rhodesmill.org/pyephem/) to compute the daily integral with a 10-min integration time step. For OCO-2, GOME-2, and GOSAT, we calculated d for each sounding and multiplied it with the instantaneous SIF during overpass to obtain the corresponding daily mean, $\overline{SIF}$. This daily-mean adjustment factor d is a first-order correction for the overpass time-induced variation in PAR (clear-sky) and thus in SIF. This correction assumes a similar fluorescence yield between 9:30 am for GOME-2 and 1:30 pm for OCO-2 (1:30 pm for GOSAT), which appears to be valid according to Zhang et al. (2018), but may require further examination in the future. Note that this correction does not account for the sun-sensor-geometry induced variations in SIF as a function of overpass time.

The daily-mean adjustment factor d varies with latitude and time (Fig. 5) because they both determine the variation of SZA and the day length. This adjustment factor has relatively weak seasonal variability in the tropics but exhibits increasingly substantial impact at higher latitudes (Fig. 5). In many current studies, the daily-mean adjustment is neglected but we emphasize here that its use can change the shape of the SIF seasonal cycle especially at higher latitudes and will also differ among instruments due to different overpass times (Fig. 4).

We used the International Satellite Land Surface Climatology Project ISLSCP Initiative II biome classification (FRIEDL et al., 2010) at a 1° × 1° spatial resolution to obtain biome specific quantities. We employed the IGBP classification scheme but combined certain classes for simplicity (following Frankenberg et al., 2011b). Specifically, evergreen and deciduous needleleaf forests were reclassified to "needleleaf forests" (denoted as NF), "grasslands" (denoted as GRA), deciduous broadleaf and mixed forests to "deciduous broadleaf forests"
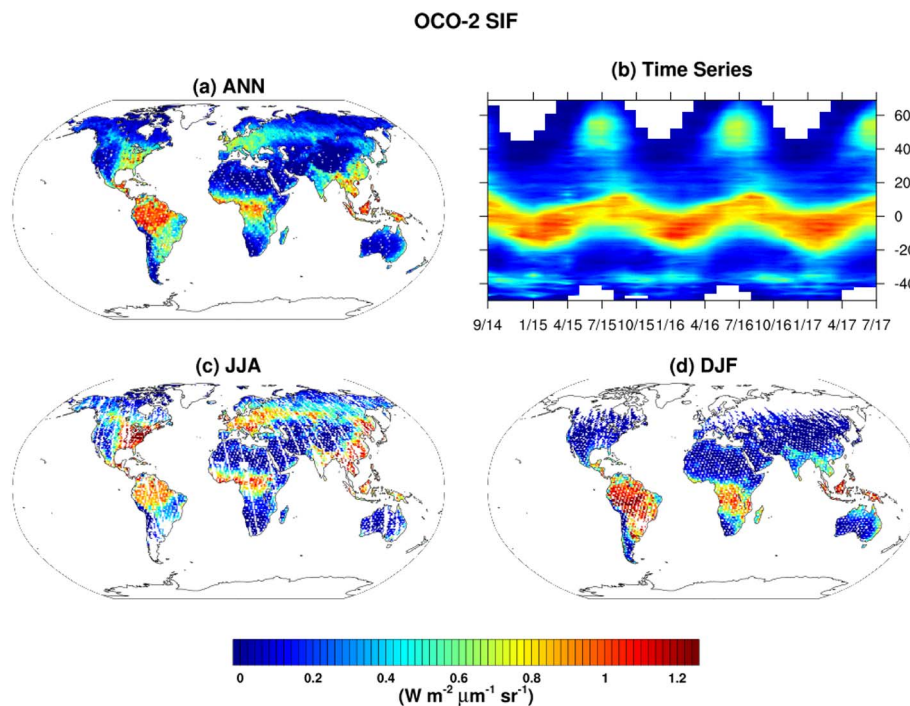
OCO-2 SIF

Fig. 6. The OCO-2 SIF retrieval (the composite of 757 nm and 771 nm) on $1^\circ \times 1^\circ$ grid for (a) the annual average, (c) the summer average (June–July–August), and (d) the winter average (December–January–February) of 2015–2016. (b) Time series of the latitudinal mean SIF since September 2014. Only grid-cells with more than five soundings are shown.
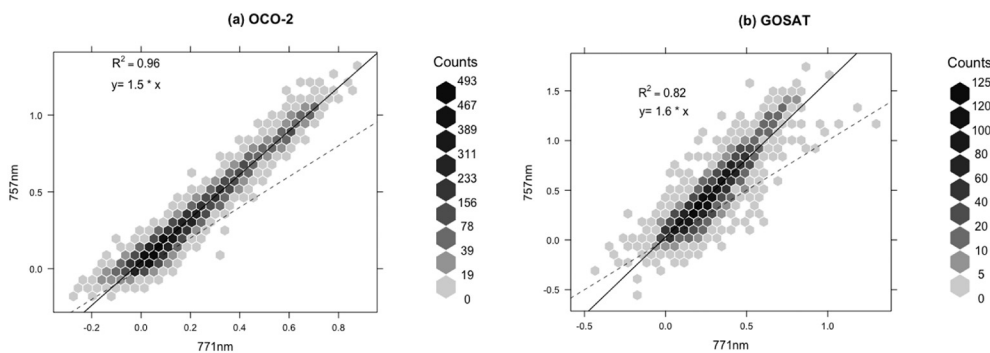

Fig. 7. The spectral relationship of SIF retrieved at different wavelengths for (a) OCO-2 and (b) GOSAT. The x- and y-axes are SIF retrievals at 757 nm and 771 nm ($Wm^{-2}\mu m^{-1} sr^{-1}$) aggregated to grid-cells ($1^\circ \times 1^\circ$ for OCO-2 and $2^\circ \times 2^\circ$ for GOSAT) averaged across the operational data collection period (since September 2014 for OCO-2 and April 2009 for GOSAT). The fitted linear regression lines passing the origin are displayed (solid), along with the 1:1 line as reference (dash). The greyscale represents the number of grid-cells in each hexagon bin. Grid-cells are discarded if $\sigma_{theo} > 0.03\,Wm^{-2}\mu m^{-1} sr^{-1}$ for OCO-2 and if $\sigma_{theo} > 0.12\,Wm^{-2}\mu m^{-1} sr^{-1}$ for GOSAT.

(denoted as DBF), closed and open shrublands to "shrublands" (denoted as SHR), woody savannas and savannas to "savannas" (denoted as SAV), croplands and cropland/natural vegetation mosaic to "croplands" (denoted as CRO).

4. Results

4.1. Global retrieval of OCO-2 SIF: spatial-temporal patterns and uncertainty assessment

The SIF products of OCO-2 retrieved during its operational data collection period exhibit expected spatial and temporal patterns (Fig. 6). The annual average of SIF (Fig. 6a) has the highest values in pan-tropics (e.g., ~1.2 $Wm^{-2}\mu m^{-1} sr^{-1}$ in rainforests in Amazon, Congo, and southeastern Asia) and approaches zero in barren regions such as the Sahara and Arabian Peninsula. The eastern US, central Europe, and southern Asia exhibit a moderate annual SIF signal (~0.6–1.0 $Wm^{-2}\mu m^{-1} sr^{-1}$). In these regions, OCO-2 SIF has substantial contributions from croplands and deciduous forests during the boreal summer (Fig. 6c). A moderate annual average of SIF emission is observed in the subtropical savannas (e.g., South America and southern Africa, Fig. 6a), which is mainly driven by higher SIF values during the austral summer (Fig. 6d).

There are pronounced seasonal variations in OCO-2 SIF (Fig. 6b). In the boreal summer, the peak in the global zonal average protrudes towards the northern hemisphere while in the austral summer, it shifts to the southern hemisphere. The extra-tropics show asymmetrical seasonal patterns between the northern and southern hemispheres. The SIF signal in the northern hemisphere (NH) has a strong seasonal cycle with a sharp peak emission in the growing season and a diminished signal during dormant months. In contrast, SIF in the extra-tropical in the southern hemisphere shows a much weaker seasonality.

The spectral relationship between SIF values retrieved at different wavelengths provides further insight into the performance of the retrieval algorithm. This is because OCO-2 SIF is retrieved independently at two micro-windows covering Fraunhofer lines with no prescribed spectral shape of SIF, as opposed to the broad window fitting for GOME-2 or SCIAMACHY. Hence, examination of the spectral relationship between 757 nm and 771 nm for all vegetated grid-cells can serve as an independent check for retrieval fidelity. Fig. 7a displays the relationship of OCO-2 SIF between 757 nm and 771 nm for all vegetated grid-cells. A strong linear relationship is observed with a $R^2 = 0.95$. The regression slope is 1.5, slightly lower than the value 1.6 for GOSAT (Fig. 7b), which is also reported by Guanter et al. (2012). Such difference may be due to a slightly different fitting window of GOSAT retrievals from OCO-2. In addition, any small but systematic retrieval
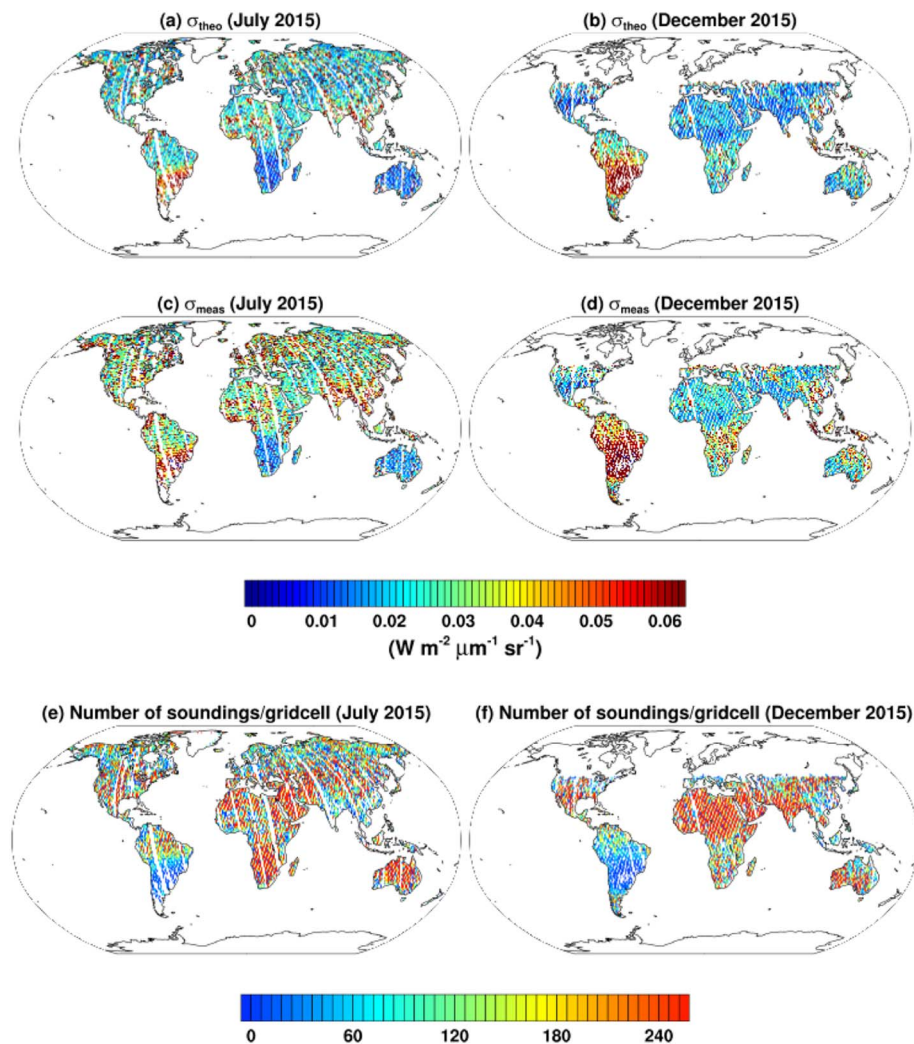
Fig. 8. The uncertainty estimates of OCO-2 SIF. (a) and (b) The theoretical estimates of the standard error of the mean, i.e., σ_{theo} (Eq. (4)) for July and December 2015, respectively. (c) and (d) the standard error of the mean σ_{meas} (Eq. (5)) estimated from real measurements. (e)–(f) The number of soundings with valid retrievals per grid-cell. Strips are due to orbital gaps in the selected months.

error at either 757 nm or 771 nm may induce variations in their ratio. Note that here we examined the spectral relationship of mean SIF by averaging it across all individual months during the operational data collection period of each mission. This relationship, or the derived slope, remains stable if only photosynthetically active months (e.g., JJA in northern hemisphere) were included.

The retrieval uncertainty of OCO-2 SIF is very low on $1° \times 1°$ (Fig. 8). For example, in almost all regions across the globe except South America, the standard error of the mean (both σ_{theo} and σ_{meas}) is generally below $0.04 \, \text{Wm}^{-2} \mu\text{m}^{-1} \text{sr}^{-1}$ (about 2% of typical peak SIF value) (Fig. 8a–d), substantially lower than the single-measurement precision $0.3–0.5 \, \text{Wm}^{-2} \mu\text{m}^{-1} \text{sr}^{-1}$ reported by Frankenberg et al. (2014). This improved precision at the grid-cell level is expected, as the retrieval error is reduced by a factor of $1/\sqrt{n}$ when n is the number of valid retrievals per grid-cell. Typically, n ranges between ~200 and ~400 within a month (Fig. 8e–f), reducing the standard error of gridded SIF by a factor of 14–20 as compared to the single measurement precision. A shift of the standard error is observed from northern to southern hemisphere, associated with the seasonal variation of the intensity of reflected light from boreal summer to austral summer. For example, southern Africa exhibits higher uncertainty in austral summer (Fig. 8a–d), because the errors in the SIF signal increase with at-sensor radiance (as photon shot-noise increases) in conjunction with a reduced number of n in this season.

South America exhibits a substantially larger uncertainty than the rest of the globe, mainly due to a much lower number of valid retrievals in this region (Fig. 8e–f). Two reasons can explain the low number of SIF retrievals in South America. First, in the vicinity of the South Atlantic Anomaly (SAA), charged energetic particles can contaminate the O_2 A band spectrometer with random spikes in different areas of the focal plane array. Currently, the SIF retrieval is excluded when these spikes occur within the range of either fitting windows as a strict filter on the reduced χ^2 is used. This strict screening of the SAA-affected observations substantially reduces the number of valid SIF retrievals. This situation will be improved with more valid retrievals becoming available in South America in the future as the SAA impact screening will be relaxed and a pre-screening of affected spectral regions will be performed, similar to the full-physics retrievals of atmospheric CO_2. Actually, the screening is more urgent for the full-physics retrievals using the full O_2 A band spectrum, which would have excluded almost all data in the South Atlantic region. The second cause is the presence of extensive thick clouds with high optical depth in wet seasons, which may reduce the number of valid retrievals, as shown by a smaller n values in December (typically < 60) relative to July. For both of these reasons, smaller values of n degrade the standard error over South America.

The uncertainty of actual measurements, σ_{meas}, is generally higher than the theoretical estimate σ_{theo} (Fig. 8c–d vs a–b). This is because
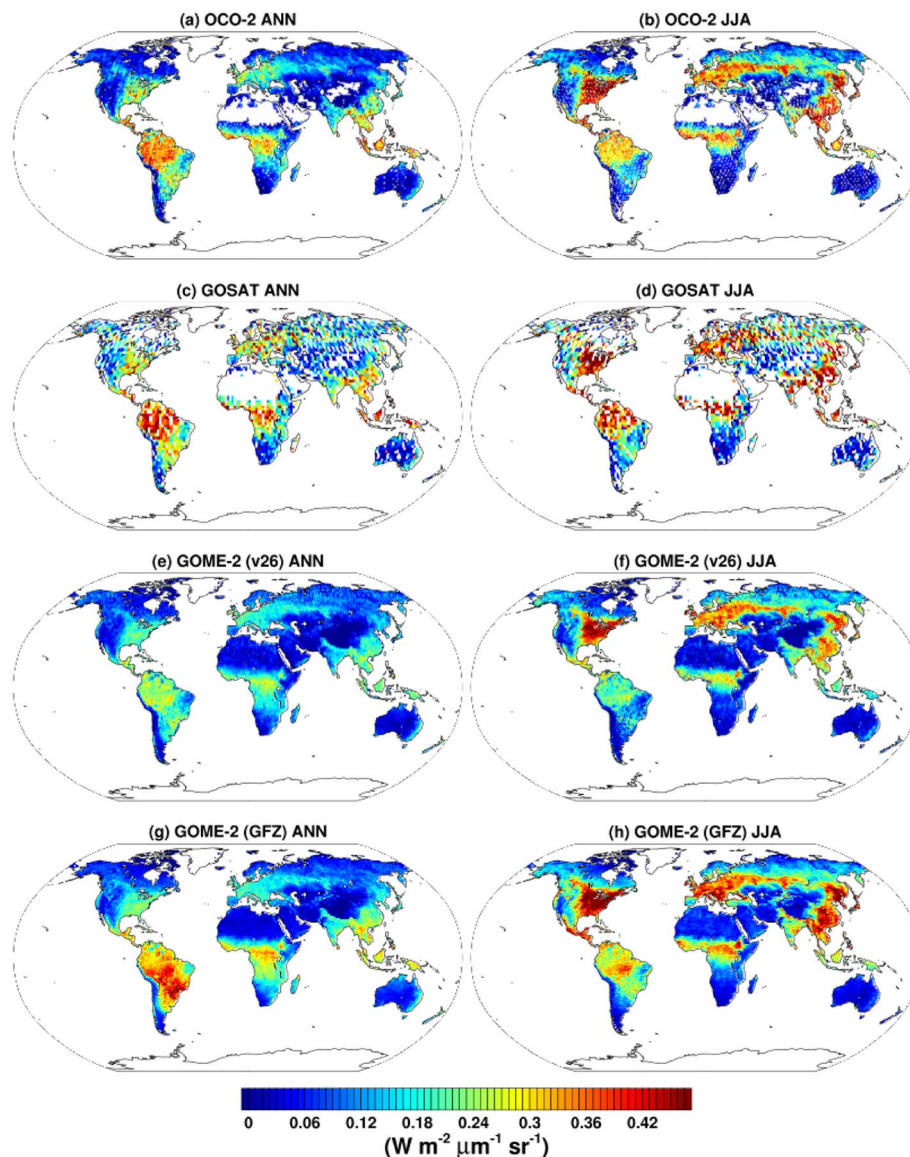
Fig. 9. Comparison of $\overline{SIF}$ (the daily-mean SIF, the product of the instantaneous SIF at local overpass and the daily-mean adjustment) among OCO-2, GOSAT, GOME-2 v26 from Joiner et al. (2013) and GOME-2 GFZ products from Köhler et al. (2015) on $1^{\circ} \times 1^{\circ}$, $2^{\circ} \times 2^{\circ}$, $0.5^{\circ} \times 0.5^{\circ}$. The left column shows the annual average of 2015 (January to December), and the right column shows the summer average (June to August in 2015). The GOME-2 SIF inferred at 740 nm is converted to the corresponding 757 nm level by multiplying a factor of 0.59, following Yang et al. (2015) and Joiner et al. (2013).

sources of uncertainty characterized by σ_{meas} include both instrumental noise and spatial-temporal variability within a grid-cell spanning in a month, while σ_{theo} quantifies only the former.

4.2. Cross-mission comparison of OCO-2 SIF with GOSAT and GOME-2 products

We compared SIF retrievals in the full year 2015 from OCO-2, GOSAT, and GOME-2 on the global scale (Fig. 9). Considering that GOME-2 SIF is inferred at 740 nm, we adjusted it to its corresponding 757 nm level using a scaling factor of 0.59, which is inferred from model simulations of Soil Canopy Observation Photochemistry and Energy fluxes (SCOPE) used by Joiner et al. (2013) and Yang et al. (2015). In addition to this wavelength correction, we applied the daily adjustment factor (Eq. (6)) to eliminate the influence of different overpass time. We found that OCO-2 and GOSAT SIF retrievals show broad spatial agreement for both annual average and boreal summer. In addition, their retrievals are on the same level of magnitude although GOSAT suffers from an obviously coarser spatial resolution due to its

sparse data acquisition. Both OCO-2 and GOSAT appear to have a higher SIF emission in the pan-tropics than GOME-2 (both v26 and GFZ products). This pattern is similar to an earlier comparison between GOME-2 and GOSAT (Joiner et al., 2013), which showed that the former retrieval is lower than the latter in the tropical rainforests. The higher OCO-2 SIF in the tropics is probably related to its smaller footprint size, which may suffer less from contamination of sub-pixel clouds as compared to a larger footprint of GOME-2. It is also possible that there is some reabsorption of SIF at 740 nm due to the generally higher chlorophyll content and more complex structures of the tropical canopies, thus the GOME-2 retrieval may be somewhat dampened with respect to the actual canopy SIF emission at this wavelength. The linear assumption between cos(SZA) and incoming solar radiation might have also contributed to the differences between OCO-2 (and also GOSAT) and GOME-2 in the tropics because such assumption is not valid under cloudy conditions which is common in tropical regions such as the Amazon. Another possibility is the different retrieval algorithms used by Joiner et al. (2013) and Köhler et al. (2015) (Fig. 9e–f vs g–h), e.g., differences in sampling the training data (non-fluorescent reference
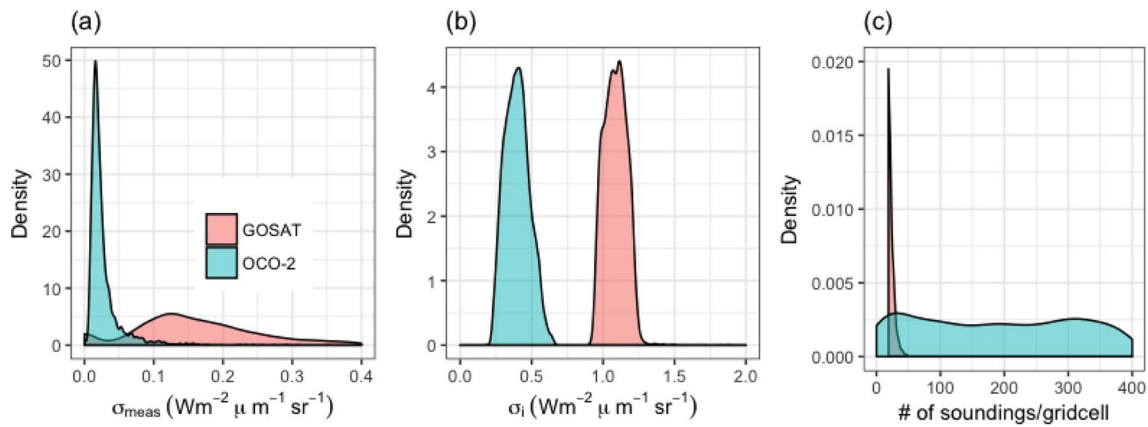
Fig. 10. Comparison between OCO-2 and GOSAT of the kernel density distribution of (a) σ_{meas} of all land grid-cells ($2^\circ \times 2^\circ$), (b) single measurement precision σ_i of all individual soundings over land, and (c) number of soundings per grid-cell in July 2015.

targets), spectral fitting windows, number of state vector elements, cloud masks, and subsequent quality filtering.

In contrast to the pan-tropics, we observed high SIF emission ($\sim$1.2–1.6 $Wm^{-2}\mu m^{-1}sr^{-1}$) at comparable intensities between OCO-2 and GOME-2 in the boreal summer in the mid- to high-latitudes of northern hemisphere, such as Eurasia and eastern US.

In addition to the cross-mission validation of SIF retrieval itself, we further compared the retrieval error between OCO-2 and GOSAT (Fig. 10). We chose GOSAT here because it has a similar overpass time and employs the same retrieval algorithm to infer SIF at wavelengths close to OCO-2. Using July 2015 as an example, we found that the probability density function (PDF) of σ_{meas} peaks at $\sim$0.03 $Wm^{-2}\mu m^{-1}sr^{-1}$ for OCO-2 retrieval and $\sim$0.12 $Wm^{-2}\mu m^{-1}sr^{-1}$ for GOSAT (Fig. 10a). The reduced retrieval error of OCO-2 is due to both the improved single retrieval precision (Fig. 10b) and the substantial increase of the number of measurement per grid-cell (Fig. 10c).

4.3. The relationship between OCO-2 SIF and GPP from regions to the globe

Comparison with GPP products confirms that the OCO-2 SIF product is able to provide a reasonable spatial depiction of plant productivity across different regions of the globe (Fig. 11). From the equator to extra-tropics, the annual mean of OCO-2 $\overline{SIF}$ in 2015 (the daily mean value converted from the instantaneous SIF at overpass) exhibits a latitudinal variation consistent with that of FLUXCOM GPP, and also with MODIS GPP except South America Andes. In addition, annual maximum OCO-2 $\overline{SIF}$ captures the US Corn belt, which is completely missing in MODIS GPP. The dry-season "greening up" or increased productivity (Huete et al., 2006) is well characterized by OCO-2 $\overline{SIF}$ along with FLUXCOM GPP. In contrast, MODIS GPP shows a decreased productivity during the same period from June to November in 2015. This large-scale comparison serves as a first-order fidelity check on OCO-2 products.

The relationship between $\overline{SIF}$ and FLUXCOM GPP is strongly linear for all biomes but the slope is not universal (Fig. 12). We performed a least-square linear regression (OLS) of FLUXCOM GPP against OCO-2 $\overline{SIF}$ and found that the regression slopes vary considerably from biome to biome. Here we forced the linear regression line to pass through the origin, because in principle zero fluorescence emission precludes any productivity. In addition to individual regressions separately done for each biome, we also performed a regression by pooling all biomes together as a global reference. Generally, croplands (CRO) and grasslands (GRA) have lowest slopes; needleleaf forests (NF) show the highest; and deciduous broadleaf forests (DBF), evergreen broadleaf forests (EBF), and savannas (SAV) have medium slopes and are close to the global reference. This biome dependence of the linear slope of OCO-2 $\overline{SIF}$ with

respect to FLUXCOM GPP appears to be similar to previous findings observed by GOSAT and GOME-2 SIF (e.g., Guanter et al., 2012; Zhang, Guanter, et al., 2016).

We further examined the seasonality of OCO-2 $\overline{SIF}$ and its consistency with FLUXCOM GPP products (Fig. 13). Considering the biome dependence of the $\overline{SIF}$-GPP linear relationship, which may also vary among different SIF products, we normalized both $\overline{SIF}$ and GPP by their corresponding seasonal maximum in order to focus on the temporal variation and phases changes of different datasets. We found that OCO-2 $\overline{SIF}$ in 2015, along with GOSAT and GOME-2 datasets, have an overall consistent seasonality with FLUXCOM GPP across different regions of the globe. For example, both $\overline{SIF}$ and FLUXCOM GPP capture the phase of the "double peak" in the Congo rainforests albeit a weaker seasonal variation of the latter variable. In addition, the phenology of croplands in the US Midwestern, North American temperate forests, Eurasian boreal forests, and southern African savannas agrees well between $\overline{SIF}$ and FLUXOM GPP. Note the Eurasian boreal forests have a smaller number of valid retrievals in the winter than summer because the high SZA observations in winter are screened out.

For the Amazonian rainforests, a gradual "green-up" from the early to end of dry season (June to November) is observed in all three $\overline{SIF}$ datasets and FLUXCOM GPP, despite a somewhat weaker seasonal swing in FLUXCOM GPP. A detailed analysis of the SIF seasonality in Amazon can be found elsewhere (Köhler et al., 2017). Here we calculated the domain average of the entire Amazon basin (10°S–2°N, 75°W–50°W) that is covered by rainforests only (Fig. 12a), but the spatial variations of the seasonal dynamics need further investigation given the high spatial heterogeneity of biogeography in this region (Xu et al., 2015). The MODIS GPP yields a distinct seasonality, e.g., a reversed seasonal pattern in Amazon, an earlier second peak in Congo, a lengthier growing season in US Midwest, and a delayed onset and shutoff of growing season in southern African savannas, compared to other datasets investigated here.

4.4. Robustness of OCO-2 SIF and GPP relationships across biomes

The SIF-GPP relationship can be potentially influenced by various factors. First, the daily adjustment factor has an asymmetrical effect on different biomes at different latitudes (Fig. 5), which may contribute to the divergence of SIF-FLUXCOM GPP slopes across biomes. Second, the regression methods may bias regression slopes if both predictors and response variables contain different levels of noise. Third, strict comparisons of gridded OCO-2 $\overline{SIF}$ with FLUXCOM GPP products require consistent temporal and spatial sampling between the two datasets. Spatial sampling bias arises from the spatial gaps between the narrow OCO-2 swaths, which leads to discontinuous spatial sampling of native SIF observations to aggregate to the $1^\circ \times 1^\circ$ grid-cell value. Frankenberg
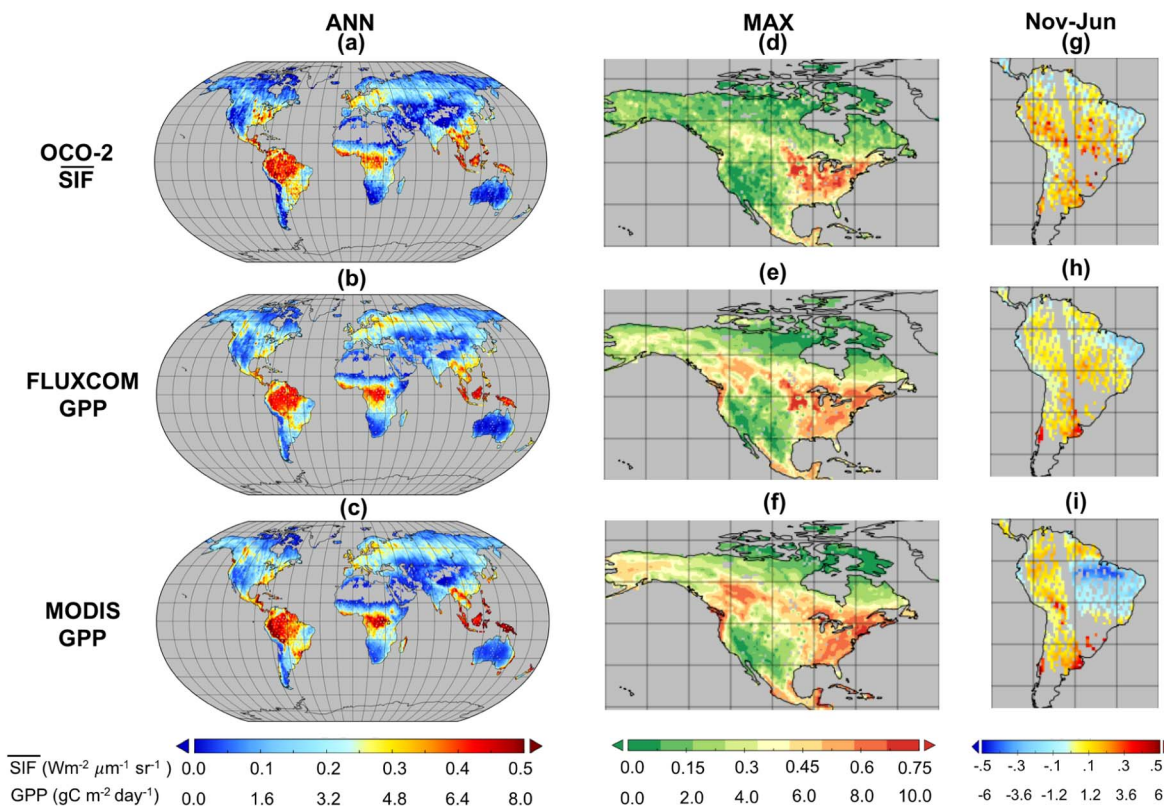
Fig. 11. The spatial pattern of OCO-2 $\overline{\text{SIF}}$ (1st row), FLUXCOM GPP (2nd row), and MODIS GPP (3rd row). (a)–(c) Show the annual average (January to December) value in 2015. The dormant months (when no SIF emission) are excluded for deriving the annual average GPP. (d)–(f) Show the annual (2015) maximum of each variable, zoomed-in to North America to highlight the US Corn belt, following Guanter et al. (2014). (g)–(i) Show the seasonal variation of each variable, zoomed-in to South America to highlight the dry-season productivity dynamics (difference between November and June in 2015) in Amazon, following Huete et al. (2006). Note Huete et al. (2006) used October as the late dry-season month, we instead use November here because of considerable OCO-2 orbital gaps in the October of 2015. Grid-cells with missing values of SIF are masked out in both GPP products in deriving annual mean, annual maximum, and seasonal changes.
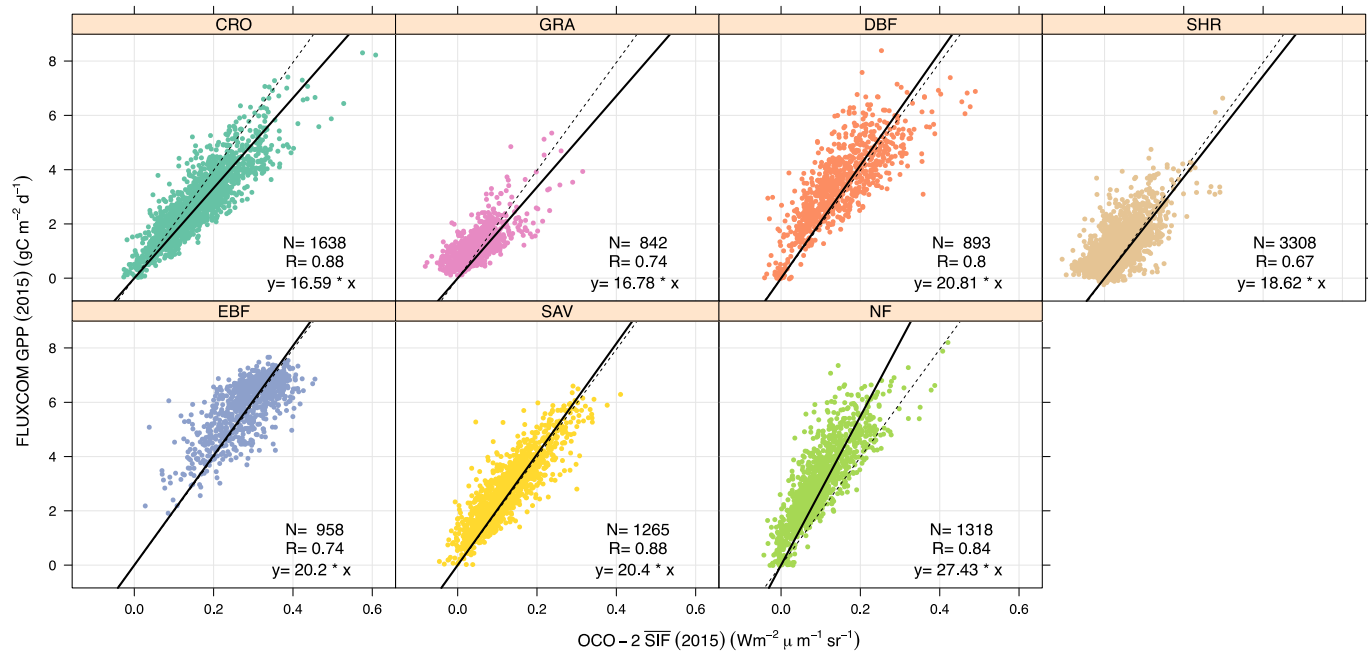

Fig. 12. The relationships between the annual mean OCO-2 $\overline{\text{SIF}}$ and FLUXCOM GPP in 2015 for different biomes. Each scatter represents a grid-cell. The fitted linear regression lines passing through the origin are displayed (solid), along with the regression line fitted with all biomes (dotted). The ordinary least square (OLS) regression is used here for the fitting. Biomes are denoted as: CRO for croplands, GRA for grasslands, DBF for deciduous broadleaf forests, SHR for shrublands, EBF for evergreen broadleaf forests, SAV for savannas, NF for needleleaf forests, respectively.
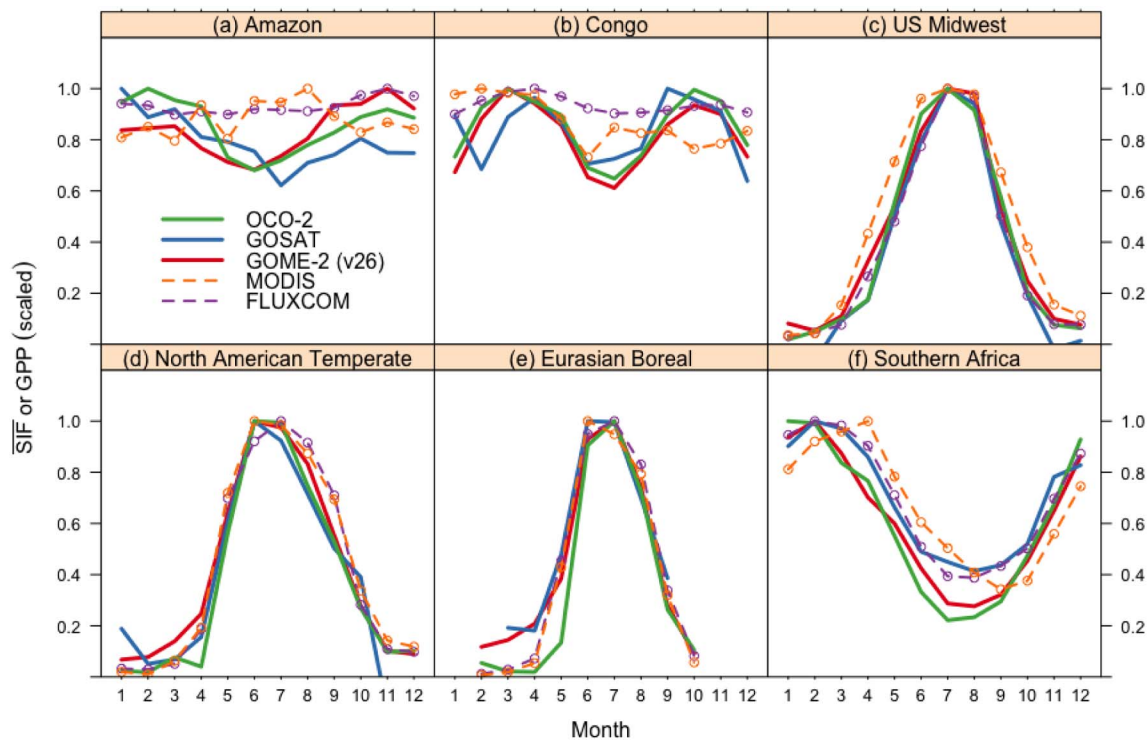
Fig. 13. The seasonal cycle of $\overline{SIF}$ and GPP at different regions (with distinct biomes) of the world. Both $\overline{SIF}$ and GPP are normalized by their corresponding seasonal maximum (thus the y-axis is unitless) to avoid applying the biome-specific $\overline{SIF}$-GPP scaling for different SIF products. All datasets are from the year 2015. The selected regions (and biomes) are: Amazon (10°S-2°N, 75°W-50°W, rainforests only), Congo (5°S-4°N, 10°E-30°E rainforests only), US Midwest (30°N-60°N, 93°W-82°W, crop only), North America Temperate (30°N-60°N, 90°W-50°W, deciduous broadleaf forests only), Eurasia (60°N-90°N, 0–180°E, needleleaf forests only), and southern Africa (30°S-5°N, 10°E-45°E, savannas only).
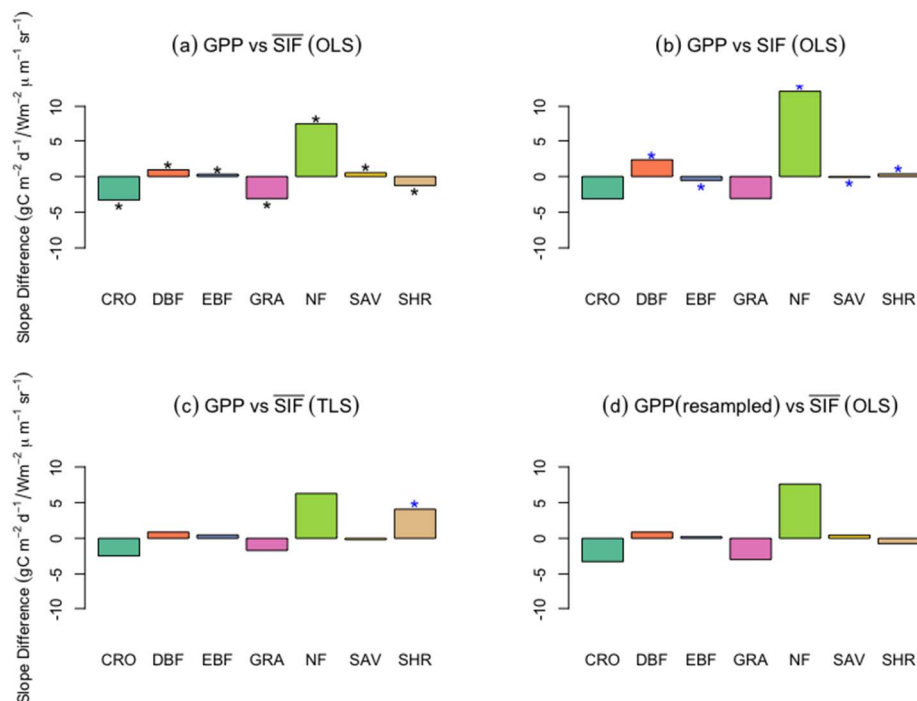

Fig. 14. Sensitivity test for robustness of the relationship between OCO-2 $\overline{SIF}$ and FLUXCOM GPP across biomes. The slope difference between the biome-specific regression (solid line in Fig. 12) and the all-biomes fitting (dotted line in Fig. 12) is used as an indicator of the consistency of $\overline{SIF}$-GPP relationships among biomes. (a) Shows the parameters obtained with ordinary least square (OLS) regression. This panel is used as the baseline to evaluate the robustness of $\overline{SIF}$-GPP relationships. (b) Checks the impact of daily adjustment factor on the slope using the instantaneous SIF values at the overpass time instead of the daily-mean $\overline{SIF}$ as in (a). The slopes here are multiplied by 3 to ensure the y-scale is comparable to other panels. (c) Examines the impact of regression methods on the slopes obtained using total least square (TLS) regression instead of OLS as in (a). (d) Evaluates the impact of spatial sampling bias resulted from OCO-2's orbital gaps. The high-resolution (0.083° × 0.083°) FLUXCOM GPP products are first resampled to pixels that are spatially co-located with $\overline{SIF}$ overpasses, and then aggregated to OCO-2 SIF resolution at 1° × 1° to construct the $\overline{SIF}$-GPP statistics. Black * in (a) indicates significant slope differences between biome-specific and all-biome fittings (significant level 0.01); blue * in (b)–(d) indicate significant differences of each test against the baseline regression in (a) (significant level 0.01). (For interpretation of the references to color in this figure legend, the reader is referred to the web version of this article.)

et al. (2014) have already shown that such bias is generally small and spatially uncorrelated, indicating that the gridded SIF has no systematic bias and therefore should represent the actual SIF intensity as if the grid-cell is fully covered by ground tracks. Here we explicitly examined the consequence of the above-mentioned factors on the $\overline{SIF}$-FLUXCOM GPP relationship across biomes (Fig. 14).

To examine the impact of daily adjustment factor, we regressed FLUXCOM GPP against the instantaneous SIF signal at OCO-2 overpass (Fig. 14b). We find that the biome dependence still holds for the relationship between OCO-2 $\overline{SIF}$ and FLUXCOM GPP, but the divergence significantly widens across biomes (except crops and grass), especially for the northern hemisphere high latitude. This indicates the importance of daily adjustment factor in determining in consistency of SIF-GPP relationships among biomes. For example, Guanter et al. (2012) used the instantaneous SIF from GOSAT and found that NF requires the highest scaling factor from SIF to a previous version of FLUXCOM GPP product among all biomes, which may be partly exacerbated by the omission of the daily adjustment factor. Also, Zhang, Guanter, et al. (2016) linked the instantaneous SIF from GOME-2 and flux tower based GPP and reported divergent SIF-GPP relationships, which may also be partly due to the omission of daily correction factor.

To examine the impact of regression methods, we performed the total least square (TLS) regression (Fig. 14c). TLS accounts for uncertainties in both predictors and response variables by minimizing errors in both directions. The regression slopes obtained from TLS exhibit small differences from the OLS regression for all biomes (except SHR), indicating that the influence of regression methods on the SIF-FLUXCOM GPP slopes is negligible.

To evaluate the spatial sampling bias resulted from OCO-2 orbital gaps (Fig. 14d), the high-resolution ($0.083° \times 0.083°$) FLUXCOM GPP products are first resampled to pixels that are spatially co-located with $\overline{SIF}$ overpasses, and then aggregated to OCO-2 SIF resolution at $1° \times 1°$ in order to construct the $\overline{SIF}$-GPP statistics. The results show that the regression slopes are not statistically significantly different between with- and without the spatial re-sampling of FLUXCOM GPP to the OCO-2 overpass, further lending us confidence that the spatial sampling bias of OCO-2 has a minimal impact on the $\overline{SIF}$-GPP relationship if assessed at large scales.

5. Discussion

5.1. Suggestions for cross-mission comparison for existing and future missions

Cross-mission comparison of SIF products helps to ensure the consistency and fidelity of different retrievals. However, such comparison is not straightforward and should be approached with caution due to different spectral, spatial, and temporal SIF sampling techniques across platforms. In this study, we applied the daily adjustment factor to all different SIF products, which serves as the first-order correction for the overpass time-induced variations in PAR. A more rigorous cross-mission comparison requires consideration of physiological variations and sun-sensor geometry changes at different overpass times that are not represented by the simple daily adjustment factor.

In the near future, OCO-2 SIF will provide a unique opportunity to cross-check the upcoming missions such as the recent launch of TROPOMI (Guanter et al., 2015) and the ESA Fluorescence Explorer (FLEX) (Drusch et al., 2017). For example, TROPOMI has some features that can be compared to OCO-2: 1) it records the radiance spectra at a 0.5 nm resolution in the 675–775 nm range, covering the Fraunhofer lines that are used for OCO-2 SIF retrieval; 2) the local overpass time of TROPOMI is ~1:30 pm, identical to that of OCO-2. These features enable a cross-check between OCO-2 and TROPOMI in a more consistent manner than the cross-mission comparison shown here. The FLEX mission is specifically designed for measuring SIF, aiming at both red and far-red retrievals (utilizing O_2-B and O_2-A band, respectively) as well as the spectrally integrated emission (Cogliati et al., 2015). As the Fraunhofer line-based retrieval is much less impacted by the O_2 re-absorption of SIF from TOC to TOA and does not require the complicated forward modeling of atmospheric radiative transfer, the robustness and accuracy of OCO-2 products can ensure a high quality benchmark for FLEX SIF products. Verrelst et al. (2016) suggested that SIF retrievals sampled at O_2 B and O_2 A bands are ideal to represent the spectrally integrated emission and to quantify GPP. Our results show that SIF retrievals sampled at individual Fraunhofer lines, which are less prone to biases induced by cloud/aerosol scattering, are very promising for tracking the spatial and temporal variations of GPP with high accuracy and precision.

In terms of spatial resolution, TROPOMI has a $7 \times 7 \, km^2$ footprint (Guanter et al., 2015), which covers multiple OCO-2 footprints. This means that multiple OCO-2 SIF retrievals will be averaged for comparison with a single TROPOMI measurement, greatly reducing the retrieval uncertainty associated with instrument noise. Importantly, OCO-2 and its successor OCO-3, TROPOMI, and FLEX will complement each other in spectral resolution, spatial coverage, data acquisition and repeat cycles. Thus, synergistic use of these products will offer an unprecedented opportunity for real-time monitoring of vegetation productivity at high spatial resolution.

5.2. Caution in interpreting the SIF-GPP relationship

Our analysis indicates that the linearity in the relationship between satellite measurements of SIF and global modeled GPP products is robust across biomes, in agreement with those with GOSAT (Guanter et al., 2012), GOME-2 (Zhang, Guanter, et al., 2016), and empirical models (Zhang, Xiao, et al., 2016). The linear relationship may be primarily driven by the shared importance of the absorbed photosynthetically active radiation (APAR, determined by both LAI and leaf chlorophyll content) for both SIF and GPP as shown in canopy-level measurements (Yang et al., 2015) and model simulations with SCOPE (Zhang, Guanter, et al., 2016). However, the linear slopes appear to vary among biomes when using the global modeled GPP product. This finding is consistent with previous studies that suggested biome-dependent SIF-GPP relationships (Guanter et al., 2012; Zhang, Guanter, et al., 2016), but different from Y. Sun et al. (2017) who complied flux tower GPP from three distinct biomes and found more convergent cross-biome SIF-GPP relationships than if the modeled GPP products were used. Y. Sun et al. (2017) suggested two possibilities for such apparent discrepancies. First, GPP cannot be measured directly and has to be either calculated with empirical models (MODIS products) or inferred from net ecosystem exchange of CO_2 and then scaled up to the globe with statistical models such as those using machine learning techniques (FLUXCOM products). Thus it is possible that the uncertainty in the estimates of global GPP products may have contributed to the divergent GPP-SIF relationships. This possibility is corroborated by Guanter et al. (2014) who showed that the flux tower-based crop productivity is nicely captured by SIF but tends to be considerably underestimated by the statistical model-based GPP products. It should be noted that the FLUXCOM GPP product has been widely used as a surrogate "truth" for global GPP, but any deviation of slopes may also be related to biases in GPP estimates, which are inherently difficult to obtain, even at flux tower sites (e.g., Wehr et al., 2016). The second possibility to consider is that the observed biome-specific relationships may indeed reflect intrinsic biochemical, physiological and canopy-structural complexities of SIF as a proxy for GPP. For example, SIF does not saturate as much as GPP at increasing light levels (Damm et al., 2015; Guanter et al., 2012). Such complexities will require the SIF-GPP relationships to be interpreted in the context of vegetation types and phenological stages as well as the broad environmental conditions to which a given vegetation is adapted. Regardless of the origins of variable SIF-GPP relationships, care must be taken when SIF is used to estimate GPP at large scales (e.g., regional and global). Even though the initial results showed a

strong empirical relationship between SIF and GPP, a more mechanistic understanding is needed. Synergistic ground measurements of SIF and GPP across biomes will offer valuable insights for understanding the mechanisms of the variations of SIF with GPP and for developing robust relationships for scaling GPP from SIF. These types of studies have already emerged with OCO-2 for a limited number of biomes, including Verma et al. (2017), Wood et al. (2017), Y. Sun et al. (2017), Li et al. (2018), but efforts are critically needed to investigate more biome types with growing records of satellite SIF measurements. Caution also needs to be taken when using OCO-2's glint or target modes because of their varying viewing geometries that can result in a directional effect on SIF emission (Guanter et al., 2012; van der Tol et al., 2009). The directional effect occurs in a way similar to the commonly observed near infrared (NIR) "hot spot" effect. It may be partly explained by chloroplast re-absorption, which differs with the upwelling transfer path when SIF escapes from canopy. Such directional effect also varies with season due to changing illumination conditions (Köhler et al., 2017). Thus integrating ground GPP with OCO-2 SIF in glint or target modes requires correction of these directional effects to exclude confounding impacts on interpreting SIF-GPP relationships (e.g., Li et al., 2018).

6. Summary

An overview is presented for the performance of OCO-2 SIF products with the initial three years' observation. This overview serves as a reference for future applications of OCO-2 SIF product. We compared OCO-2 SIF with existing retrievals from GOSAT and GOME-2 and further investigated its relationship with multiple GPP products for different biomes. Our results demonstrated that the OCO-2 SIF closely resembles the spatial pattern of FLUXCOM GPP from the equator to extra-tropics in both hemispheres, but the estimated linear relationships vary in slope across biomes when investigated using global modeled GPP products. Further studies are needed to explain the root causes of such variations. Comparison of OCO-2 SIF with GOME-2 SIF reveals that these two products differ disproportionally between the tropics and the NH high-latitude. Recommendations on applications of OCO-2 SIF and cross-comparison with other satellite missions were discussed.

Acknowledgement

References

Cogliati, S., Verhoef, W., Kraft, S., Sabater, N., Alonso, L., Vicent, J., Moreno, J., Drusch, M., Colombo, R., 2015. Retrieval of sun-induced fluorescence using advanced spectral fitting methods. Remote Sens. Environ. 169, 344–357.

Damm, A., Guanter, L., Paul-Limoges, E., van der Tol, C., Hueni, A., Buchmann, N., Eugster, W., Ammann, C., Schaepman, M.E., 2015. Far-red sun-induced chlorophyll fluorescence shows ecosystem-specific relationships to gross primary production: an assessment based on observational and modeling approaches. Remote Sens. Environ. 166, 91–105.

Drusch, M., Moreno, J., Del Bello, U., Franco, R., Goulas, Y., Huth, A., Kraft, S., Middleton, E.M., Miglietta, F., Mohammed, G., Nedbal, L., Rascher, U., Schuttemeyer, D., Verhoef, W., 2017. The FLuorescence EXplorer mission concept—ESA's earth explorer 8. IEEE Trans. Geosci. Remote Sens. 55, 1273–1284. http://dx.doi.org/10.1109/TGRS.2016.2621820.

Frankenberg, C., Butz, A., Toon, G.C., 2011a. Disentangling chlorophyll fluorescence from atmospheric scattering effects in O 2 A-band spectra of reflected sun-light. Geophys. Res. Lett. 38http://dx.doi.org/10.1029/2010GL045896. (n/a–n/a).

Frankenberg, C., Fisher, J.B., Worden, J., Badgley, G., Saatchi, S.S., Lee, J.-E., Toon, G.C., Butz, A., Jung, M., Kuze, A., Yokota, T., 2011b. New global observations of the terrestrial carbon cycle from GOSAT: patterns of plant fluorescence with gross primary productivity. Geophys. Res. Lett. 38http://dx.doi.org/10.1029/2011GL048738. (n/a–n/a).

Frankenberg, C., O'Dell, C., Guanter, L., McDuffie, J., 2012. Remote sensing of near-infrared chlorophyll fluorescence from space in scattering atmospheres: implications for its retrieval and interferences with atmospheric CO 2 retrievals. Atmos. Meas. Tech. 5, 2081–2094.

Frankenberg, C., O'Dell, C., Berry, J., Guanter, L., Joiner, J., Köhler, P., Pollock, R., Taylor, T.E., 2014. Prospects for chlorophyll fluorescence remote sensing from the Orbiting Carbon Observatory-2. Remote Sens. Environ. 147, 1–12. http://dx.doi.org/10.1016/j.rse.2014.02.007.

FRIEDL, M.A., STRAHLER, A.H., HODGES, J., 2010. ISLSCP II MODIS (Collection 4) IGBP Land Cover, 2000–2001. http://dx.doi.org/10.3334/ornldaac/968.

Guanter, L., Frankenberg, C., Dudhia, A., Lewis, P.E., Gómez-Dans, J., Kuze, A., Suto, H., Grainger, R.G., 2012. Retrieval and global assessment of terrestrial chlorophyll fluorescence from GOSAT space measurements. Remote Sens. Environ. 121, 236–251. http://dx.doi.org/10.1016/j.rse.2012.02.006.

Guanter, L., Zhang, Y., Jung, M., Joiner, J., Voigt, M., Berry, J.A., Frankenberg, C., Huete, A.R., Zarco-Tejada, P., Lee, J.-E., Moran, M.S., Ponce-Campos, G., Beer, C., Camps-Valls, G., Buchmann, N., Gianelle, D., Klumpp, K., Cescatti, A., Baker, J.M., Griffis, T.J., 2014. Global and time-resolved monitoring of crop photosynthesis with chlorophyll fluorescence. Proc. Natl. Acad. Sci. U. S. A. 111, E1327–33. http://dx.doi.org/10.1073/pnas.1320008111.

Guanter, L., Aben, I., Tol, P., Krijger, J.M., Hollstein, A., Köhler, P., Damm, A., Joiner, J., Frankenberg, C., Landgraf, J., 2015. Potential of the TROPOspheric monitoring instrument (TROPOMI) onboard the Sentinel-5 Precursor for the monitoring of terrestrial chlorophyll fluorescence. Atmos. Meas. Tech. 8, 1337–1352. http://dx.doi.org/10.5194/amt-8-1337-2015.

Huete, A.R., Didan, K., Shimabukuro, Y.E., Ratana, P., Saleska, S.R., Hutyra, L.R., Yang, W., Nemani, R.R., Myneni, R., 2006. Amazon rainforests green-up with sunlight in dry season. Geophys. Res. Lett. 33, L06405. http://dx.doi.org/10.1029/2005GL025583.

Joiner, J., Yoshida, Y., Vasilkov, A.P., Corp, L.A., Middleton, E.M., 2011. First observations of global and seasonal terrestrial chlorophyll fluorescence from space. Biogeosciences 8, 637–651. http://dx.doi.org/10.5194/bg-8-637-2011.

Joiner, J., Yoshida, Y., Vasilkov, A.P., Middleton, E.M., Campbell, P.K.E., Kuze, A., Corp, L.A., 2012. Filling-in of near-infrared solar lines by terrestrial fluorescence and other geophysical effects: simulations and space-based observations from SCIAMACHY and GOSAT. Atmos. Meas. Tech. 5, 809–829.

Joiner, J., Guanter, L., Lindstrot, R., Voigt, M., Vasilkov, A.P., Middleton, E.M., Huemmrich, K.F., Yoshida, Y., Frankenberg, C., 2013. Global monitoring of terrestrial chlorophyll fluorescence from moderate-spectral-resolution near-infrared satellite measurements: methodology, simulations, and application to GOME-2. Atmos. Meas. Tech. 6, 2803–2823. http://dx.doi.org/10.5194/amt-6-2803-2013.

Joiner, J., Yoshida, Y., Guanter, L., Middleton, E.M., 2016. New methods for retrieval of chlorophyll red fluorescence from hyper-spectral satellite instruments: simulations and application to GOME-2 and SCIAMACHY. Atmos. Meas. Tech. Discuss. 1–41.

Jung, M., Reichstein, M., Margolis, H.A., Cescatti, A., Richardson, A.D., Arain, M.A., Arneth, A., Bernhofer, C., Bonal, D., Chen, J., Gianelle, D., Gobron, N., Kiely, G., Kutsch, W., Lasslop, G., Law, B.E., Lindroth, A., Merbold, L., Montagnani, L., Moors, E.J., Papale, D., Sottocornola, M., Vaccari, F., Williams, C., 2011. Global patterns of land-atmosphere fluxes of carbon dioxide, latent heat, and sensible heat derived from eddy covariance, satellite, and meteorological observations. J. Geophys. Res. Biogeosci. 116.

Köhler, P., Guanter, L., Joiner, J., 2015. A linear method for the retrieval of sun-induced chlorophyll fluorescence from GOME-2 and SCIAMACHY data. Atmos. Meas. Tech. 8, 2589–2608. http://dx.doi.org/10.5194/amt-8-2589-2015.

Köhler, P., Guanter, L., Kobayashi, H., Walther, S., Yang, W., 2017. Assessing the potential of sun-induced fluorescence and the canopy scattering coefficient to track large-scale vegetation dynamics in Amazon forests. Remote Sens. Environ. http://dx.doi.org/10.1016/j.rse.2017.09.025.

Li, X., Xiao, J., He, B., 2018. Chlorophyll fluorescence observed by OCO-2 is strongly related to gross primary productivity estimated from flux towers in temperate forests. Remote Sens. Environ. http://dx.doi.org/10.1016/j.rse.2017.09.034.

Plascyk, J.A., Gabriel, F.C., 1975. The Fraunhofer line discriminator MKII-an airborne instrument for precise and standardized ecological luminescence measurement. IEEE Trans. Instrum. Meas. 24 (4), 306–313.

Sun, Y., Frankenberg, C., Wood, J.D., Schimel, D.S., Jung, M., Guanter, L., Drewry, D.T., Verma, M., Porcar-Castell, A., Griffis, T.J., Gu, L., Magney, T.S., Köhler, P., Evans, B., Yuen, K., 2017. OCO-2 advances photosynthesis observation from space via solar-induced chlorophyll fluorescence. Science. http://dx.doi.org/10.1126/science.aam5747. (80–.).

Sun, K., Liu, X., Nowlan, C.R., Cai, Z., Chance, K., Frankenberg, C., Lee, R.A.M., Pollock, R., Rosenberg, R., Crisp, D., 2017. Characterization of the OCO-2 instrument line shape functions using on-orbit solar measurements. Atmos. Meas. Tech. http://dx.doi.org/10.5194/amt-10-939-2017.

Taylor, T.E., O'Dell, C.W., Frankenberg, C., Partain, P.T., Cronk, H.Q., Savtchenko, A., Nelson, R.R., Rosenthal, E.J., Chang, A.Y., Fisher, B., Osterman, G.B., Pollock, R.H., Crisp, D., Eldering, A., Gunson, M.R., 2016. Orbiting Carbon Observatory-2 (OCO-2) cloud screening algorithms: validation against collocated MODIS and CALIOP data. Atmos. Meas. Tech. http://dx.doi.org/10.5194/amt-9-973-2016.

van der Tol, C., Verhoef, W., Timmermans, J., Verhoef, a., Su, Z., 2009. An integrated model of soil-canopy spectral radiances, photosynthesis, fluorescence, temperature and energy balance. Biogeosciences 6, 3109–3129.

Tramontana, G., Jung, M., Camps-valls, G., Ichii, K., Raduly, B., 2016. Predicting Carbon Dioxide and Energy Fluxes Across Global FLUXNET Sites with Regression Algorithms. pp. 4291–4313. http://dx.doi.org/10.5194/bg-2015-661.

Vasilkov, A., Joiner, J., Spurr, R., 2013. Note on rotational-Raman scattering in the O2A-and B-bands. Atmos. Meas. Tech. http://dx.doi.org/10.5194/amt-6-981-2013.

Verma, M., Schimel, D., Evans, B., Frankenberg, C., Beringer, J., Drewry, D.T., Magney, T., Marang, I., Hutley, L., Moore, C., Eldering, A., 2017. Effect of environmental

conditions on the relationship between solar-induced fluorescence and gross primary productivity at an OzFlux grassland site. J. Geophys. Res. Biogeosci. http://dx.doi.org/10.1002/2016JG003580.

Verrelst, J., van der Tol, C., Magnani, F., Sabater, N., Rivera, J.P., Mohammed, G., Moreno, J., 2016. Evaluating the predictive power of sun-induced chlorophyll fluorescence to estimate net photosynthesis of vegetation canopies: a SCOPE modeling study. Remote Sens. Environ. 176, 139–151. http://dx.doi.org/10.1016/j.rse.2016.01.018.

Wehr, R., Munger, J.W., McManus, J.B., Nelson, D.D., Zahniser, M.S., Davidson, E.A., Wofsy, S.C., Saleska, S.R., 2016. Seasonality of temperate forest photosynthesis and daytime respiration. Nature 534, 680–683. http://dx.doi.org/10.1038/nature17966.

Wolanin, A., Rozanov, V.V., Dinter, T., Noël, S., Vountas, M., Burrows, J.P., Bracher, A., 2015. Global retrieval of marine and terrestrial chlorophyll fluorescence at its red peak using hyperspectral top of atmosphere radiance measurements: feasibility study and first results. Remote Sens. Environ. http://dx.doi.org/10.1016/j.rse.2015.05.018.

Wood, J.D., Griffis, T.J., Baker, J.M., Frankenberg, C., Verma, M., Yuen, K., 2017. Multiscale analyses of solar-induced florescence and gross primary production. Geophys. Res. Lett. 44, 533–541. http://dx.doi.org/10.1002/2016GL070775.

Xu, L., Saatchi, S.S., Yang, Y., Myneni, R.B., Frankenberg, C., Chowdhury, D., Bi, J., 2015. Satellite observation of tropical forest seasonality: spatial patterns of carbon exchange in Amazonia. Environ. Res. Lett. 10, 084005.

Yang, X., Tang, J., Mustard, J.F., Lee, J.E., Rossini, M., Joiner, J., Munger, J.W., Kornfeld, A., Richardson, A.D., 2015. Solar-induced chlorophyll fluorescence that correlates with canopy photosynthesis on diurnal and seasonal scales in a temperate deciduous forest. Geophys. Res. Lett. 42, 2977–2987.

Zhang, Y., Guanter, L., Berry, J.A., van der Tol, C., Yang, X., Tang, J., Zhang, F., 2016. Model-based analysis of the relationship between sun-induced chlorophyll fluorescence and gross primary production for remote sensing applications. Remote Sens. Environ. http://dx.doi.org/10.1016/j.rse.2016.10.016.

Zhang, Y., Xiao, X., Jin, C., Dong, J., Zhou, S., Wagle, P., Joiner, J., 2016. Remote sensing of environment consistency between sun-induced chlorophyll fluorescence and gross primary production of vegetation in North America. Remote Sens. Environ. 183, 154–169. http://dx.doi.org/10.1016/j.rse.2016.05.015.

Zhang, Y., Xiao, X.M., Zhang, Y.G., Wolf, S., Zhou, S., Joiner, J., Guanter, L., Verma, M., Sun, Y., Yang, X., Paul-Limoges, E., Gough, C.M., Wohlfahrt, G., Gioli, B., van der Tol, C., Yann, N., Lund, M., de Grandcourt, A., 2018. On the relationship between sub-daily instantaneous and daily total gross primary production: implications for interpreting satellite-based SIF retrievals. Remote Sens. Environ. 205, 276–289.

Zhao, M., Running, S.W., 2010. Drought-induced reduction in global terrestrial net primary production from 2000 through 2009. Science 329, 940–943. http://dx.doi.org/10.1126/science.1192666. (80–.).